

Gauged Q-ball dark matter through a cosmological first-order phase transition

Siyu Jiang^a Fa Peng Huang^{1a} Pyungwon Ko^b

^a*MOE Key Laboratory of TianQin Mission, TianQin Research Center for Gravitational Physics & School of Physics and Astronomy, Frontiers Science Center for TianQin, Gravitational Wave Research Center of CNSA, Sun Yat-sen University (Zhuhai Campus), Zhuhai 519082, China*

^b*School of Physics, Korea Institute for Advanced Study, Seoul 02455, Korea*

E-mail: jiangsy36@mail2.sysu.edu.cn, huangfp8@mail.sysu.edu.cn,
pko@kias.re.kr

ABSTRACT: As a new type of dynamical dark matter mechanism, we discuss the stability of the gauged Q-ball dark matter and its production mechanism through a cosmological first-order phase transition. This work delves into the study of gauged Q-ball dark matter generated during the cosmic phase transition. We demonstrate detailed discussions on the stability of gauged Q-balls to rigorously constrain their charge and mass ranges. Additionally, employing analytic approximations and the mapping method, we provide qualitative insights of gauged Q-ball. We establish an upper limit on the gauge coupling constant and give the relic density of stable gauged Q-ball dark matter formed during a first-order phase transition. Furthermore, we discuss potential observational signatures or constraints of gauged Q-ball dark matter, including astronomical observations and gravitational wave signals.

KEYWORDS: Phase Transitions in the Early Universe; Models for Dark Matter

¹Corresponding author.

Contents

1	Introduction	1
2	Gauged Q-ball	3
2.1	Friedberg-Lee-Sirlin-Maxwell model	3
2.2	Numerical results of the field configuration, energy, and charge	6
3	Basic properties of gauged Q-balls	8
3.1	dE/dQ for gauged Q-balls	8
3.2	Stability of gauged Q-balls	9
3.2.1	Quantum mechanical stability	9
3.2.2	Stress stability	10
3.2.3	Stability against fission	12
3.2.4	Classical stability	12
4	Thin-wall approximation	14
4.1	Piecewise model	15
4.2	Mapping gauged Q-balls	16
4.3	Maximal charge and energy of gauged Q-balls: analytic approximations	18
5	Gauged Q-ball DM from electroweak FOPT	20
5.1	Electroweak FOPT	20
5.2	Bubble wall filtering during FOPT	22
5.3	Charge of Q-ball in the electroweak FOPT	23
5.4	Relic density of gauged Q-ball DM	26
6	Constraints and detection of gauged Q-ball DM	28
6.1	Direct detection and astronomical constraints	28
6.2	Phase transition GW	29
7	Discussion and conclusion	31

1 Introduction

Exploring the nature of dark matter (DM) is one of the central issues in (astro)particle physics and cosmology [1]. So far, there are no expected signals of conventional DM candidates like Weakly Interacting Massive Particles (WIMPs) in the DM direct detection and collider search experiments [2–4]. Then simple WIMP scenarios are strongly disfavored. There are a number of ways to save WIMP scenarios. For example, DM may have substantial couplings only to the 3rd generation fermions [5–7], or dark sectors may consists of two

or more stable DM species (see, for example, [8]). Or one can discard WIMP scenarios and consider other possibilities for DM productions and annihilations or decays in the early Universe. This status motivates us to study ultralight or ultra heavy DM candidate (for reviews, see Refs. [9, 10]).

Solitons produced in the early Universe are natural candidates of heavy DM (see, for example, [11] for hidden sector monopole DM accompanied by stable spin-1 vector DM and massless dark radiation, and Ref. [12] for hunting for topological DM using atomic clocks). These solitons are specific field configurations which are classified into two classes, namely, the topological solitons and the non-topological solitons. Recently, as renaissance of the quark nuggets DM proposed by Witten [13], various new ideas on the non-topological soliton DM are proposed, where the DM relic density can be produced by the dynamical process of cosmological first-order phase transition (FOPT), such as the Q-ball DM [14–17]. These new mechanisms can naturally avoid the unitarity problem for heavy DM [18]. Dynamical DM mechanisms are specified by the DM penetration behavior into the bubble which depends on the DM mass and bubble wall velocity [19, 20].

There are extensive discussions on the non-topological solitons in a theory of complex scalar field with global $U(1)$ symmetry, proposed in [21] and known as Q-balls [22]. And it is natural to study the Q-balls in the gauged case [22–30], by promoting the global $U(1)$ symmetry to the local gauge $U(1)$ symmetry. For reviews of $U(1)$ gauged Q-balls, see [31–33]. Q-balls have been proposed as a potential DM candidate in supersymmetric theories [34, 35]. They can also explain the baryon asymmetry of the Universe [36]. The gauged Q-ball DM in supersymmetry model has also been studied in several papers [37, 38]. It is meaningful to search for other production mechanisms without supersymmetry of Q-ball or gauged Q-ball DM. In this paper, we study whether the $U(1)$ gauged Q-balls produced during cosmic phase transition could be a viable DM candidate. If the gauged Q-ball can be stable under certain circumstances, we still need some mechanism to (1) produce the charge asymmetry (i.e. locally produce lots of same charge particles to form Q-ball) (2) and packet the same sign charges in the small size after overcoming the Coulomb repulsive interaction. For the first condition, the primordial charge asymmetry could be produced by some early Universe processes such as decays of heavier particles. Cosmological FOPT can naturally realize the second condition and can produce phase transition gravitational wave (GW) which can be detected by future GW experiments, such as LISA [39], TianQin [40, 41], Taiji [42], BBO [43], DECIGO [44], and Ultimate-DECIGO [45].

In this work, for the first time, we study the natural production mechanism of gauged Q-ball DM through a cosmological FOPT. The paper is organised as follows. We describe the basic model that can produce the gauged Q-balls and the numerical solutions of the Q-ball profiles in section 2. Basic properties and the stable parameter space of gauged Q-balls are discussed in section 3. Thin-wall approximation and the corresponding analytic evaluations are given in section 4. Phase transition dynamics in the Standard Model (SM) plus an extra singlet and the relic density of gauged Q-ball DM are elucidated in section 5. Signals and constraints of gauged Q-ball DM are given in section 6. Concise conclusions and discussions are given in section 7.

2 Gauged Q-ball

2.1 Friedberg-Lee-Sirlin-Maxwell model

In this work, we adopt the Friedberg-Lee-Sirlin two-component model [26]¹ plus gauge component, which is called Friedberg-Lee-Sirlin-Maxwell (FLSM) model [25]. This model and the corresponding stability of $U(1)$ gauged Q-ball have been discussed in [23, 25, 48–50]. We begin our discussions with the following Lagrangian density

$$\mathcal{L} = (D_\mu \phi)^\dagger (D^\mu \phi) + \frac{1}{2} \partial_\mu h \partial^\mu h - \frac{1}{4} \tilde{A}_{\mu\nu} \tilde{A}^{\mu\nu} - V(\phi, h) , \quad (2.1)$$

where the potential $V(\phi, h)$ reads

$$V(\phi, h) = \frac{\lambda_{\phi h}}{2} h^2 |\phi|^2 + \frac{\lambda_h}{4} (h^2 - v_0^2)^2 . \quad (2.2)$$

ϕ and h are the complex scalar field and (real) Higgs field respectively. $D_\mu = \partial_\mu + i\tilde{g}\tilde{A}_\mu$ and $\tilde{A}_{\mu\nu} = \partial_\mu \tilde{A}_\nu - \partial_\nu \tilde{A}_\mu$ where \tilde{A}_μ is a dark $U(1)$ gauge field and \tilde{g} is the corresponding gauge coupling constant. \tilde{A}_μ can be identified as the dark electromagnetic field. We fix the Higgs mass $m_h = 125$ GeV and vacuum expectation value $v_0 = 246$ GeV at zero temperature then $\lambda_h = m_h^2/(2v_0^2) \approx 0.13$. The complex scalar ϕ gains mass through the portal coupling with the Higgs. In the true vacuum, $m_\phi = \sqrt{\frac{\lambda_{\phi h}}{2}} v_0$. We assume $\lambda_{\phi h} > 0$, and thus the Lagrangian density is symmetric under the dark $U(1)$ symmetry which remains unbroken when the Universe goes through the electroweak phase transition. The local $U(1)$ gauge symmetry leads to the conserved current,

$$J_\mu = i \left(\phi^\dagger \overleftrightarrow{\partial}_\mu \phi + 2i\tilde{g}\tilde{A}_\mu |\phi|^2 \right) , \quad (2.3)$$

and the corresponding conserved charge,

$$Q = \int d^3x J^0 . \quad (2.4)$$

Once the gauged Q-balls are formed in this FLSM model, one could consider a coherent configuration of ϕ , h , and \tilde{A}_μ at a given charge Q . The lowest energy state will have no “magnetic field” so the space component $\tilde{A}_i = 0$ [23, 25]. We assume spherical symmetry for the lowest energy configuration. Scaling away the physical dimensions, we introduce dimensionless field variables \mathcal{A} , Φ , and \mathcal{H} defined in the convention of Ref. [25].

$$\tilde{A}_t(r) = v_0 \frac{\tilde{g}}{\sqrt{2\lambda_h}} \mathcal{A}(\rho), \quad \phi(r) = \frac{v_0}{\sqrt{2}} \Phi(\rho) e^{-i\omega t}, \quad h(r) = v_0 \mathcal{H}(\rho) , \quad (2.5)$$

where $\rho \equiv \sqrt{2\lambda_h} v_0 r = m_h r$. The Lagrangian, with the substitution of the field variables defined above, becomes

$$L = -4\pi \frac{v_0}{\sqrt{2\lambda_h}} \int d\rho \rho^2 \left[\frac{1}{2} (\nu - \alpha^2 \mathcal{A})^2 \Phi^2 - \frac{1}{8} (\mathcal{H}^2 - 1)^2 - \frac{k^2}{2} \mathcal{H}^2 \Phi^2 - \frac{1}{2} (\partial_\rho \Phi)^2 - \frac{1}{2} (\partial_\rho \mathcal{H})^2 + \frac{\alpha^2}{2} (\partial_\rho \mathcal{A})^2 \right] , \quad (2.6)$$

¹The Friedberg-Lee-Sirlin two-component model has been reviewed in details in Refs. [46, 47].

where $\alpha \equiv \frac{|\tilde{g}|}{\sqrt{2\lambda_h}}$, $k \equiv \frac{\sqrt{\lambda_{\phi h}}}{2\sqrt{\lambda_h}} = \frac{m_\phi}{m_h}$, and $\nu \equiv \frac{\omega}{\sqrt{2\lambda_h}v_0}$. By varying L with respect to \mathcal{A} , Φ , and \mathcal{H} , we find the equations of motion (EoM) for the three fields,

$$\frac{1}{\rho^2} \partial_\rho (\rho^2 \partial_\rho \mathcal{A}) + (\nu - \alpha^2 \mathcal{A}) \Phi^2 = 0 , \quad (2.7)$$

$$\frac{1}{\rho^2} \partial_\rho (\rho^2 \partial_\rho \Phi) + [(\nu - \alpha^2 \mathcal{A})^2 - k^2 \mathcal{H}^2] \Phi = 0 , \quad (2.8)$$

and

$$\frac{1}{\rho^2} \partial_\rho (\rho^2 \partial_\rho \mathcal{H}) - k^2 \mathcal{H} \Phi^2 - \frac{1}{2} \mathcal{H} (\mathcal{H}^2 - 1) = 0 . \quad (2.9)$$

The total energy is given by

$$E = \frac{4\pi v_0}{\sqrt{2\lambda_h}} \int d\rho \rho^2 \mathcal{E} , \quad (2.10)$$

where $\mathcal{E} = \frac{\alpha^2}{2} (\partial_\rho \mathcal{A})^2 + \frac{1}{2} (\partial_\rho \Phi)^2 + \frac{1}{2} (\partial_\rho \mathcal{H})^2 + \frac{1}{2} [(\nu - \alpha^2 \mathcal{A})^2 + k^2 \mathcal{H}^2] \Phi^2 + \frac{1}{8} (\mathcal{H}^2 - 1)^2$. And the total charge is given by

$$Q = \frac{2\pi}{\lambda_h} \int d\rho \rho^2 (\nu - \alpha^2 \mathcal{A}) \Phi^2 . \quad (2.11)$$

From Eqs. (2.7) and (2.11) we see that

$$\frac{\lambda_h Q}{2\pi} = - \lim_{\rho \rightarrow \infty} 4\pi \rho^2 \partial_\rho \mathcal{A} . \quad (2.12)$$

Therefore we get, for large ρ , $\mathcal{A} \rightarrow \frac{\lambda_h Q}{2\pi\rho}$ or $\tilde{A}_t \rightarrow \frac{\tilde{g}Q}{4\pi r}$. Then Eq. (2.8) at large ρ becomes

$$\frac{1}{\rho^2} \partial_\rho (\rho^2 \partial_\rho \Phi) - \frac{2\nu \tilde{g}^2 Q}{4\pi\rho} \Phi + (\nu^2 - k^2) \Phi = 0 . \quad (2.13)$$

It has been shown in Ref. [32] for $\nu < k$ that this equation at $\rho \rightarrow \infty$ has the solution of the form,

$$\Phi(\rho) = C_U e^{-\sqrt{k^2 - \nu^2} \rho} U \left(1 + \frac{\nu \tilde{g}^2 Q}{4\pi \sqrt{k^2 - \nu^2}}, 2, 2\sqrt{k^2 - \nu^2} \rho \right) , \quad (2.14)$$

where C_U is a constant and $U(a, b, z)$ is the confluent hypergeometric function of the second kind. For $\sqrt{k^2 - \nu^2} \rho \gg 1$ we get

$$\Phi(\rho) \sim \rho^{-1 - \frac{\nu \tilde{g}^2 Q}{4\pi \sqrt{k^2 - \nu^2}}} e^{-\sqrt{k^2 - \nu^2} \rho} . \quad (2.15)$$

We can see that in the limit $\tilde{g} \rightarrow 0$ this form coincides with the nongauged global Q-ball, $\Phi(\rho) \sim \rho^{-1} e^{-\sqrt{k^2 - \nu^2} \rho}$. The difference is caused by taking into account the dark electromagnetic potential $\mathcal{A}(\rho)$. For $\omega = m_\phi$ or $\nu = k$, Eq. (2.13) takes the form of

$$\frac{1}{\rho^2} \partial_\rho (\rho^2 \partial_\rho \Phi) - \frac{2k \tilde{g}^2 Q}{4\pi\rho} \Phi = 0 . \quad (2.16)$$

The solution to this equation reads $\Phi(\rho) = C_K \frac{K_1\left(\sqrt{\frac{2k\tilde{g}^2 Q}{\pi}}\rho\right)}{\sqrt{\rho}}$, where C_K is a constant and $K_1(z)$ is the modified Bessel function of the second kind. For large ρ this solution has the form of $\Phi(\rho) \sim \rho^{-\frac{3}{4}} e^{-\sqrt{\frac{2k\tilde{g}^2 Q}{\pi}}\rho}$. This also differs from the global case, in which one expects $\Phi(\rho) \sim \frac{1}{\rho}$ for $\nu = k$. For the case $\nu > k$, it can be seen from Eq. (2.13) that the corresponding solutions for the complex scalar field are oscillatory at $\rho \rightarrow \infty$, leading to unexpected infinite charge and energy. We think these solutions are unphysical and should be discarded.

It is convenient to write Eq. (2.7) in the form

$$\partial_\rho (\rho^2 \partial_\rho \mathcal{A}) = -(\nu - \alpha^2 \mathcal{A}) \Phi^2 \rho^2 . \quad (2.17)$$

Suppose that $\mathcal{A}(0) > \nu/\alpha^2$. Eq. (2.17) then implies that $\rho^2 \partial_\rho \mathcal{A}$ is an increasing function of ρ such that $\partial_\rho \mathcal{A} > 0$ and $\mathcal{A}(\rho) > \nu/\alpha^2$ for all $\rho > 0$. This possibility is not acceptable, given that $\nu > 0$ and $\mathcal{A}(\rho) \rightarrow 0$ at $\rho \rightarrow \infty$. The only acceptable possibility is that $\mathcal{A}(0) \leq \nu/\alpha^2$. Then $\partial_\rho \mathcal{A} < 0$ and therefore $\mathcal{A}(\rho)$ is a monotonically decreasing function of ρ . We can then say that $\mathcal{A}(\rho)$ obeys the inequalities

$$0 \leq \alpha^2 \mathcal{A}(\infty) \leq \alpha^2 \mathcal{A}(\rho) \leq \alpha^2 \mathcal{A}(0) \leq \nu \leq k . \quad (2.18)$$

The energy integral Eq. (2.10) can be written in a different form. Demanding that the Lagrangian (2.6) is stationary at $\epsilon = 1$ under the rescaling of the form $\rho \rightarrow \epsilon \rho$, leads to the relation $dL(\rho \rightarrow \epsilon \rho)/d\epsilon|_{\epsilon=1} = 0$, this gives the relation:

$$\begin{aligned} & 3 \int d\rho \rho^2 \left[\frac{1}{2} (\nu - \alpha^2 \mathcal{A})^2 \Phi^2 - \frac{1}{8} (\mathcal{H}^2 - 1)^2 - \frac{1}{2} \mathcal{H}^2 \Phi^2 k^2 \right] \\ &= \int d\rho \rho^2 \left[\frac{1}{2} (\partial_\rho \Phi)^2 + \frac{1}{2} (\partial_\rho \mathcal{H})^2 - \frac{\alpha^2}{2} (\partial_\rho \mathcal{A})^2 \right] . \end{aligned} \quad (2.19)$$

Substituting Eqs. (2.19) and (2.7) into Eq. (2.10), one obtains

$$\begin{aligned} E &= \frac{4\pi v_0}{\sqrt{2\lambda_h}} \int d\rho \left[(\nu - \alpha^2 \mathcal{A})^2 \Phi^2 + \frac{1}{3} (\partial_\rho \Phi)^2 + \frac{1}{3} (\partial_\rho \mathcal{H})^2 + \frac{2\alpha^2}{3} (\partial_\rho \mathcal{A})^2 \right] \\ &= \frac{4\pi v_0}{\sqrt{2\lambda_h}} \int d\rho \left[-(\nu - \alpha^2 \mathcal{A}) \partial_\rho (\rho^2 \partial_\rho \mathcal{A}) + \rho^2 \left\{ \frac{1}{3} (\partial_\rho \Phi)^2 + \frac{1}{3} (\partial_\rho \mathcal{H})^2 + \frac{2\alpha^2}{3} (\partial_\rho \mathcal{A})^2 \right\} \right] \\ &= \omega Q + \frac{4\pi}{3} \frac{v_0}{\sqrt{2\lambda_h}} \int d\rho \rho^2 \left[(\partial_\rho \Phi)^2 + (\partial_\rho \mathcal{H})^2 - \alpha^2 (\partial_\rho \mathcal{A})^2 \right] , \end{aligned} \quad (2.20)$$

where in the third line we have integrated by part and use the fact that $\rho^2 \partial_\rho \mathcal{A} \rightarrow -\frac{\tilde{g}^2 Q}{4\pi\alpha^2}$ and $\mathcal{A} \rightarrow 0$ at large ρ . We can see that the energy for the free field solution when we neglect the variation of Φ and \mathcal{H} takes the form

$$E_{\text{free}} = m_\phi Q + \text{“dark electrostatic energy”} . \quad (2.21)$$

The “dark electrostatic energy” is roughly proportional to $\frac{\tilde{g}^2 Q^2}{R}$ for charges uniformly distributed on scale R .

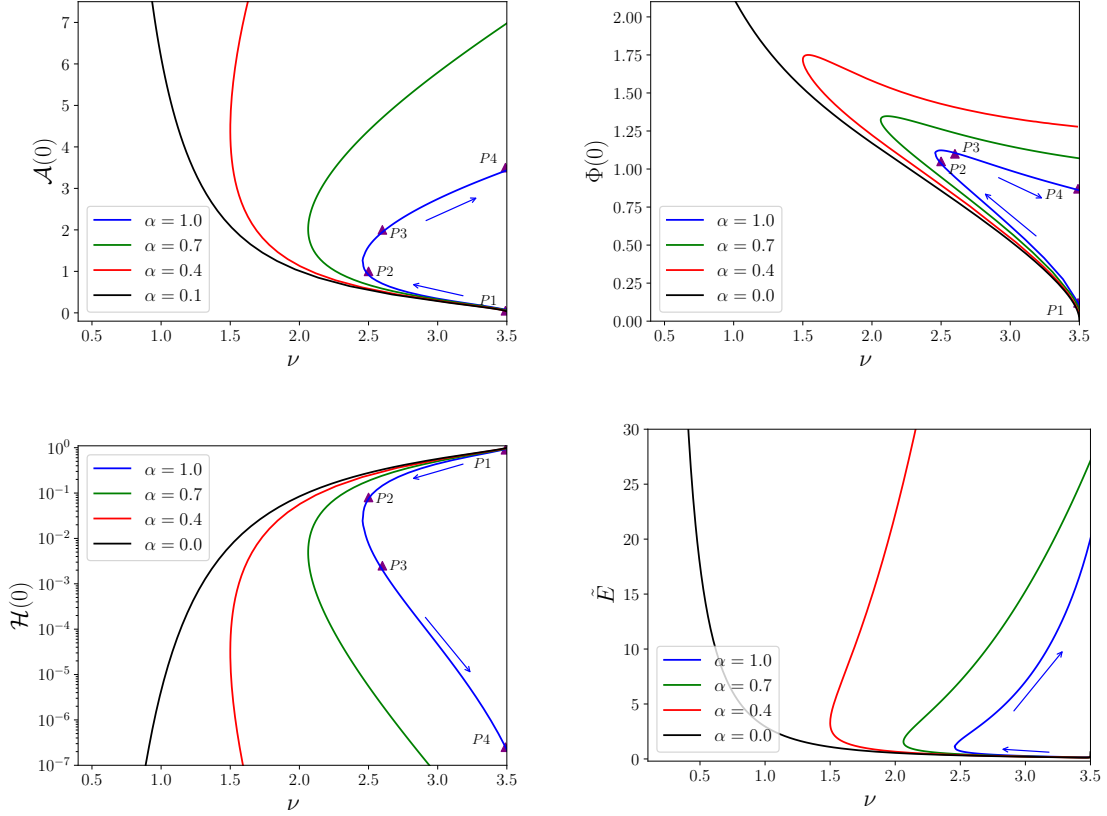


Figure 1. Values of the three fields at the Q-ball center and the total energy \tilde{E} for different values of gauge coupling α . The arrows represent the evolution of the frequency ν . We choose $k = 3.5$ which corresponds to $\lambda_{\phi h} \approx 6$. Four specific solutions $P1, P2, P3, P4$ for $\alpha = 1.0$ are marked by the triangles and the corresponding profiles are shown in figure 2.

2.2 Numerical results of the field configuration, energy, and charge

After qualitative analysis of the gauged Q-ball solution, we begin to numerically solve Eqs. (2.7), (2.8), and (2.9) with the following boundary conditions,

$$\frac{\partial \mathcal{A}}{\partial \rho} = \frac{\partial \Phi}{\partial \rho} = \frac{\partial \mathcal{H}}{\partial \rho} = 0 \text{ at } \rho = 0, \quad \mathcal{A} = \Phi = 0 \text{ and } \mathcal{H} = 1 \text{ at } \rho = \infty. \quad (2.22)$$

The first boundary condition is necessary so that the terms $\frac{2}{\rho} \left(\frac{\partial \mathcal{A}}{\partial \rho} \right)$, $\frac{2}{\rho} \left(\frac{\partial \Phi}{\partial \rho} \right)$, and $\frac{2}{\rho} \left(\frac{\partial \mathcal{H}}{\partial \rho} \right)$ do not become singular at $\rho = 0$, and the latter is necessary because the energy density \mathcal{E} and charge density $(\nu - \alpha^2 \mathcal{A})\Phi^2$ should be integrable over the infinite spatial volume and the integral should be finite.

It is convenient to introduce the dimensionless quantities for the total energy and

charge of the gauged Q-ball,

$$\begin{aligned}\tilde{E} &\equiv \frac{\lambda_h}{2\pi m_\phi} E = \frac{1}{k} \int_0^\infty d\rho \rho^2 \mathcal{E} , \\ \tilde{Q} &\equiv \frac{\lambda_h Q}{2\pi} = \int_0^\infty d\rho \rho^2 (\nu - \alpha^2 \mathcal{A}) \Phi^2 ,\end{aligned}\tag{2.23}$$

which can be calculated directly once the numerical solutions of the corresponding differential equations are found.

We use the relaxation method [51, 52] to solve coupled 2nd order ordinary differential equations, Eqs. (2.7), (2.8) and (2.9), with boundary conditions, Eq. (2.22). The relaxation method solves the boundary value problems by updating the trial functions on the grid in an iterative way. As an example, we fix $k = 3.5$ and we scan over all of the solutions at a given value of α . The results can be seen from figure 1. The frequency ν firstly decreases in the direction of the arrow. We call this the “first branch” where the back reaction of gauge field is small. Then the solutions turn on the “second branch” where ν increases and the gauge field dominates. Contrary to the global Q-ball, the parameter ν does not uniquely determine the charge and energy of the gauged Q-ball. For the global case, the energy and charge increase as the ν approaches zero. However, in the case of gauged Q-ball, the ν is replaced by $\nu - \alpha^2 \mathcal{A}$. Then on the second branch where the gauge field \mathcal{A} dominates, ν has to increase in order to satisfy $\nu - \alpha^2 \mathcal{A} > 0$.

We choose four specific solutions $P1, P2, P3, P4$ in figure 1 for $\alpha = 1.0$ which are marked by the purple triangles and the corresponding numerical profiles of \mathcal{A} , Φ and \mathcal{H} are shown in figure 2. We can see that as the value of $\mathcal{A}(0)$ of the gauged Q-ball becomes larger, the Higgs field value inside the Q-ball is closer to zero. Actually, when the value of $\mathcal{A}(0)$ becomes larger, the radius, charge and energy also increase, so we can say that the Higgs value is effectively zero inside large gauged Q-balls.

The total charge of gauged Q-ball for different values of gauge coupling α is shown in the left panel of figure 3. It can be seen that the charge for the gauged Q-ball is also finite at a nonzero α . However, for the global Q-ball the charge is unbounded from above. In order to obtain a gauged Q-ball with relatively large charge, the gauge coupling has to be small enough.

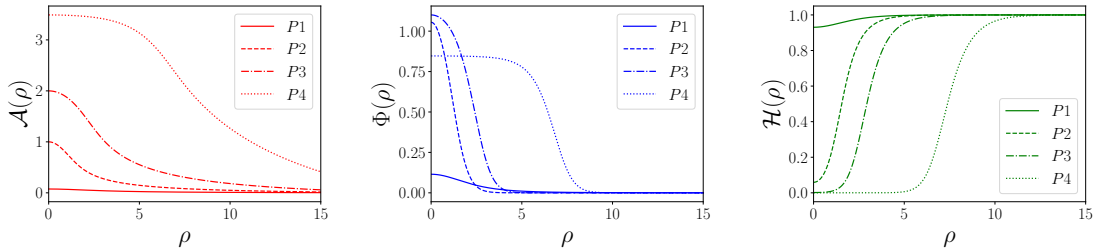


Figure 2. Profiles of the dark gauge field, complex scalar field, Higgs field of the gauged Q-ball. Here we choose the marked points $P1, P2, P3, P4$ in figure 1 where $k = 3.5$ and $\alpha = 1.0$.

We can define two typical radius for the Higgs field $\mathcal{H}(\rho)$ and the Q-ball field $\Phi(\rho)$ respectively. The ρ_\star is defined by $\mathcal{H}(\rho_\star) = 1/2$ and ρ_b is defined by $\Phi(\rho_b) = \Phi(0)/2$. These

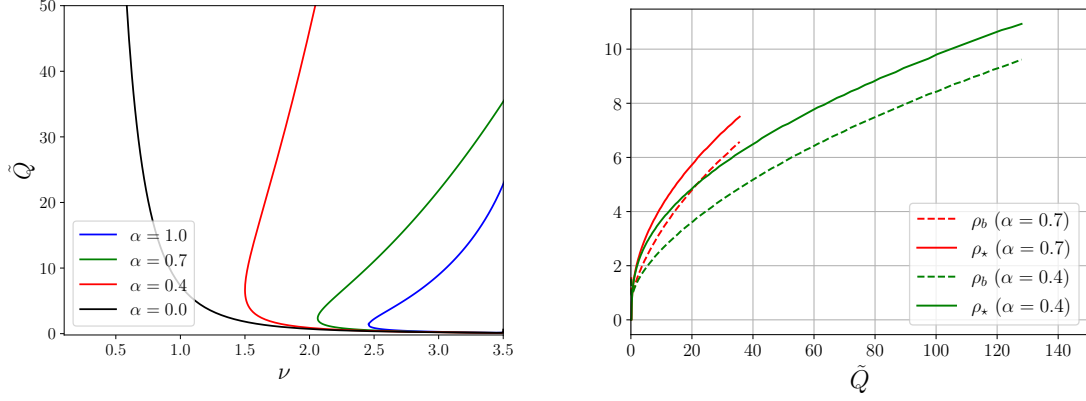


Figure 3. Left: total charge \tilde{Q} for different values of α for $U(1)$ gauged Q-balls. Right: the two typical radius for the Q-ball field $\Phi(\rho)$ and Higgs field $\mathcal{H}(\rho)$.

two radius are shown in the right panel of figure 3. It can be seen that ρ_\star is generally larger than ρ_b . One may prefer to call ρ_\star the radius of the “Higgs ball”. Hereafter, we use ρ_\star to represent the Q-ball radius which defines the charge and energy of gauged Q-balls.

3 Basic properties of gauged Q-balls

3.1 dE/dQ for gauged Q-balls

It is well known that for non-gauged Q-balls the relations $dE/dQ = \omega$ holds. Here we will show that this also holds for gauged Q-balls in FLSM model. From Eq. (2.10), we have

$$\begin{aligned} \frac{dE}{d\nu} = & \frac{4\pi v_0}{\sqrt{2\lambda_h}} \int d\rho \rho^2 \left\{ \alpha^2 (\partial_\rho \mathcal{A}) \left(\partial_\rho \frac{d\mathcal{A}}{d\nu} \right) + (\partial_\rho \Phi) \left(\partial_\rho \frac{d\Phi}{d\nu} \right) + (\partial_\rho \mathcal{H}) \left(\partial_\rho \frac{d\mathcal{H}}{d\nu} \right) \right. \\ & + \left[\left(1 - \alpha^2 \frac{d\mathcal{A}}{d\nu} \right) (\nu - \alpha^2 \mathcal{A}) + k^2 \mathcal{H} \frac{d\mathcal{H}}{d\nu} \right] \Phi^2 + [(\nu - \alpha^2 \mathcal{A})^2 + k^2 \mathcal{H}^2] \Phi \frac{d\Phi}{d\nu} \\ & \left. + \frac{1}{2} (\mathcal{H}^2 - 1) \mathcal{H} \frac{d\mathcal{H}}{d\nu} \right\}. \end{aligned} \quad (3.1)$$

After integrating $\partial_\rho \Phi$ and $\partial_\rho \mathcal{H}$ by part and using Eqs. (2.8) and (2.9), we can get

$$\begin{aligned} \frac{dE}{d\nu} = & \frac{4\pi v_0}{\sqrt{2\lambda_h}} \int d\rho \rho^2 \left[\alpha^2 (\partial_\rho \mathcal{A}) \left(\partial_\rho \frac{d\mathcal{A}}{d\nu} \right) + (\nu - \alpha^2 \mathcal{A}) \left(1 - \alpha^2 \frac{d\mathcal{A}}{d\nu} \right) \Phi^2 + 2(\nu - \alpha^2 \mathcal{A})^2 \Phi \frac{d\Phi}{d\nu} \right] \\ = & \frac{4\pi v_0}{\sqrt{2\lambda_h}} \int d\rho \rho^2 \left\{ (\nu - \alpha^2 \mathcal{A}) \frac{d}{d\nu} [(\nu - \alpha^2 \mathcal{A}) \Phi^2] + \alpha^2 (\partial_\rho \mathcal{A}) \left(\partial_\rho \frac{d\mathcal{A}}{d\nu} \right) \right\} \\ = & \sqrt{2\lambda_h} v_0 \nu \frac{dQ}{d\nu} + \underbrace{\frac{4\pi v_0}{\sqrt{2\lambda_h}} \int d\rho \rho^2 \left\{ -\alpha^2 \mathcal{A} \frac{d}{d\nu} [(\nu - \alpha^2 \mathcal{A}) \Phi^2] + \alpha^2 (\partial_\rho \mathcal{A}) \left(\partial_\rho \frac{d\mathcal{A}}{d\nu} \right) \right\}}_{=0}. \end{aligned} \quad (3.2)$$

In the third line we have integrated $\partial_\rho \mathcal{A}$ by part and used Eq. (2.7), then the integral vanishes. Finally,

$$\frac{dE}{d\omega} = \frac{dE}{d\nu} \frac{d\nu}{d\omega} = \left(\sqrt{2\lambda_h} v_0 \omega \frac{dQ}{d\omega} \right) \left(\frac{1}{\sqrt{2\lambda_h} v_0} \right) = \omega \frac{dQ}{d\omega}, \quad (3.3)$$

which leads to

$$\frac{dE}{dQ} = \omega \quad (3.4)$$

for $\frac{dQ}{d\omega} \neq 0$. The existence of $\frac{dQ}{d\omega} = 0$ indicates the locally minimal or locally maximal charge.

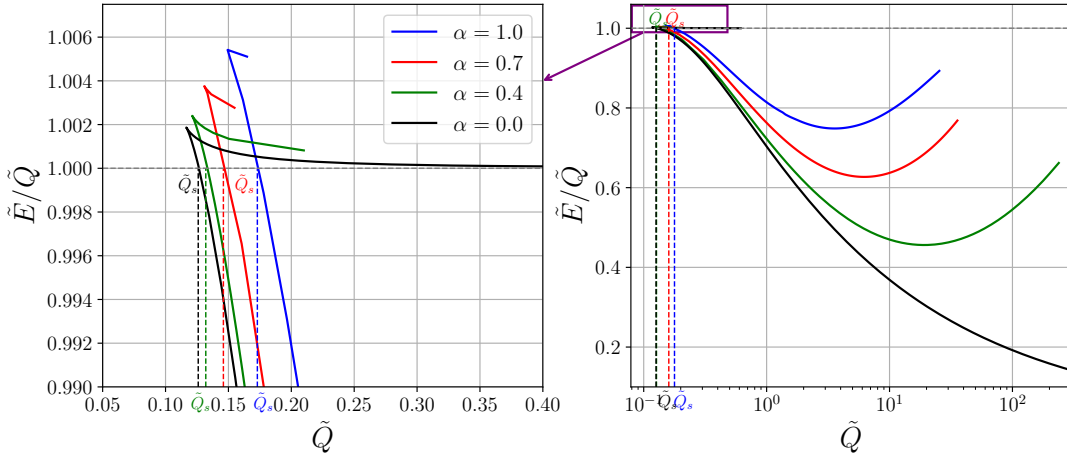


Figure 4. The energy over charge \tilde{E}/\tilde{Q} for different values of α . The \tilde{Q}_s represents the value of charge which satisfies $\tilde{E}/\tilde{Q} = 1$.

3.2 Stability of gauged Q-balls

The stability of the Q-ball is an important criterion to judge whether it can serve as the DM candidate. Unlike the global Q-balls, the stability of gauged Q-balls is still being discussed. In this subsection, we will systematically analyze four stability criteria of gauged Q-balls and show the viable parameter space of stable gauged Q-balls.

3.2.1 Quantum mechanical stability

The quantum mechanical stability is satisfied if

$$E < m_\phi Q \quad \text{or} \quad \tilde{E}/\tilde{Q} < 1. \quad (3.5)$$

This means that the gauged Q-ball is stable against decay to free scalar particles. It should be noted that if the Q-ball has decay channels into other fundamental scalar particles which have the mass m_i that are smaller than m_ϕ , we need to replace m_ϕ by m_i in Eq. (3.5). The decay of global Q-balls or gauged Q-balls has been discussed in several works [36, 53–55].

When the effective energy of DM particles inside the gauged Q-balls $\pi/r_\star \propto (\omega - \tilde{g}\tilde{A}_t)$ is larger than the masses of decay products, the decay process is kinetically allowed. In our case, the gauged Q-balls decay mainly through the process $\phi^\dagger\phi \rightarrow hh$. However, as the Q-ball radius r_\star is large enough or $(\omega - \tilde{g}\tilde{A}_t)$ is small, the gauged Q-balls are stable against decaying into 125 GeV Higgs particles.

The ratio \tilde{E}/\tilde{Q} is shown in the figure 4. As the frequency $\nu \rightarrow k$ on the first branch, there is a region of parameter space where $\tilde{E}/\tilde{Q} > 1$. It implies the existence of a minimal Q-ball charge \tilde{Q}_s defined as $\tilde{E}(\tilde{Q}_s)/\tilde{Q}_s = 1$ of the quantum mechanically stable gauged Q-ball. We can see from figure 4 that for the global Q-balls the \tilde{E}/\tilde{Q} decreases with growing \tilde{Q} when $\tilde{E}/\tilde{Q} < 1$. The branch of $\tilde{E}/\tilde{Q} > 1$ corresponds to $\nu \rightarrow k$. So the global Q-balls are quantum mechanically stable as $\nu \ll k$ and $\tilde{Q} > \tilde{Q}_s$. One would wonder that the gauged Q-ball will destroy the quantum mechanical stability at large charge because the dark electrostatic energy is proportional to \tilde{Q}^2 and thus the \tilde{E}/\tilde{Q} is proportional to \tilde{Q} . However, we found the gauged Q-balls is always quantum mechanically stable on the second branch where the gauge field dominates because of the charge of the gauged Q-balls must be finite.

3.2.2 Stress stability

Now we investigate the effect of the electrostatic repulsion on the stability of the gauged Q-balls. In Ref. [49], the authors pointed out that, just like the hadrons, a necessary condition for stability of the configuration of gauged Q-balls is the balance of the internal forces, called von Laue condition [56, 57]

$$\int_0^\infty dr r^2 p(r) = 0 . \quad (3.6)$$

Here $p(r)$ is the radial distribution of the pressure inside the Q-ball, which can be extracted from the energy-momentum tensor by using the following parametrization [58, 59]:

$$T_{ij} = \left(\hat{r}_i \hat{r}_j - \frac{1}{3} \delta_{ij} \right) s(r) + \delta_{ij} p(r) . \quad (3.7)$$

$s(r)$ is the traceless part which yields the anisotropy of pressure (shear forces). This kind of stability has also been studied on global Q-balls [59, 60].

One stronger local constraint is that the normal force per unit area acting on an infinitesimal area element at a distance r , must be directed outward [60, 61],

$$F(r) = \frac{2}{3} s(r) + p(r) > 0 . \quad (3.8)$$

This is a necessary but not sufficient condition for stability. By using the rescaled parameters, we have the expressions of $p(\rho)$ and $s(\rho)$ in the FLSM model:

$$\begin{aligned} p(\rho) &= 2\lambda_h v_0^4 \left[-\frac{1}{6} (\partial_\rho \Phi)^2 - \frac{1}{6} (\partial_\rho \mathcal{H})^2 + \frac{\alpha^2}{6} (\partial_\rho \mathcal{A})^2 + \frac{1}{2} (\nu - \alpha^2 \mathcal{A})^2 \Phi^2 - \frac{k^2}{2} \Phi^2 \mathcal{H}^2 - \frac{1}{8} (\mathcal{H}^2 - 1)^2 \right] , \\ s(\rho) &= 2\lambda_h v_0^4 \left[(\partial_\rho \Phi)^2 + (\partial_\rho \mathcal{H})^2 - \alpha^2 (\partial_\rho \mathcal{A})^2 \right] , \end{aligned} \quad (3.9)$$

from which we get

$$F(\rho) = 2\lambda_h v_0^4 \left[\frac{1}{2}(\partial_\rho \Phi)^2 + \frac{1}{2}(\partial_\rho \mathcal{H})^2 - \frac{\alpha^2}{2}(\partial_\rho \mathcal{A})^2 + \frac{1}{2}(\nu - \alpha^2 \mathcal{A})^2 \Phi^2 - \frac{k^2}{2} \Phi^2 \mathcal{H}^2 - \frac{1}{8}(\mathcal{H}^2 - 1)^2 \right]. \quad (3.10)$$

In figure 5, we show the profile of $F(\rho)$ for four marked points in figure 1. We can see that the $F(\rho)$ has no nodes for $P1$ and $P2$ on the first branch. $F(\rho)$ has negative values on the second branch so the gauged Q-balls on the second branch where gauge potential dominates are unstable. It should be noted that the inequality (3.8) takes an approximation that Q-balls behave as a continuous media, which needs more discussions.

The stress-stability is the most stringent stability criterion in this work. We are not sure if the gauged Q-ball on the second branch would decay into free particles or smaller Q-balls. And it is meaningful to explore that how we can get rid of the strong constraints from stress-stability, in other words, how to get large gauged Q-balls with large gauge coupling. Maybe we can consider an example where two scalar case where the two scalars ϕ and ψ possess opposite charges. If the electrostatic field produced by the two scalars cancels with each other, which implies

$$\tilde{g}Q_\phi + \tilde{g}'Q_\psi = 0, \quad (3.11)$$

where \tilde{g} and \tilde{g}' are the gauge couplings of ϕ and ψ respectively, this guarantees the electric neutrality of the interior of the gauged Q-balls [62, 63]. The gauged Q-balls will avoid the electric repulsion which leads to the stress-instability even the gauge coupling is large. We expect these Q-balls can also be the DM candidate because they will behave as the ordinary global Q-balls.

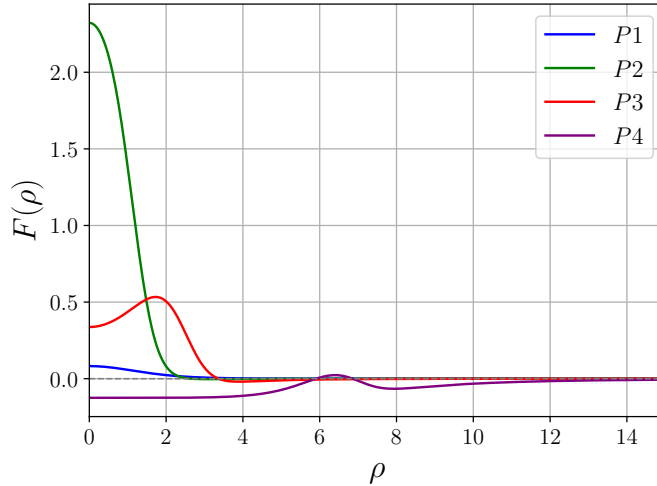


Figure 5. Profile of $F(\rho)$ defined by Eq. (3.10) for the four marked points in figure 1.

3.2.3 Stability against fission

For global (i.e., nongauged) Q-balls the corresponding stability criterion against fission takes the form

$$d^2E/dQ^2 < 0 . \quad (3.12)$$

This clearly leads to $E(Q_1) + E(Q_2) > E(Q_1 + Q_2)$ when $E(0) = 0$. However, this may not hold everywhere for the gauged Q-balls due to the presence of the gauge potential. In Ref. [31] the authors gave a detailed discussion on the stability against fission of $U(1)$ gauged Q-balls. They pointed out that we could not make any conclusion about the stability against fission for gauged Q-balls on the second branch. Nevertheless, it has been shown that the gauged Q-balls on the first branch are generally stable because the back-reaction of the gauge field is generally small.

3.2.4 Classical stability

The problem of classical stability of $U(1)$ gauged Q-balls is discussed in detail in Ref. [64]. The classical stability criterion was firstly derived in [65] for one-field Q-balls and was discussed for the model with two scalar fields in [26]. The proof of Refs. [26, 65] was based on examining the properties of the energy functional of the system. Instead, the examination of Ref. [64] is based on the Vakhitov-Kolokolov method [66, 67] which utilized linearized EoM for the perturbations above the background solution.

We only consider the spherical perturbations on the gauged Q-ball. We adopt the following ansatz:

$$\begin{aligned} \phi(t, r) &= e^{-i\omega t} f(r) + e^{-i\omega t} e^{\gamma t} (u(r) + il(r)) , \\ \tilde{A}_t(t, r) &= \tilde{A}_t(r) + e^{\gamma t} a_0(r) , \\ h(t, r) &= h(r) + e^{\gamma t} \sigma(r) , \end{aligned} \quad (3.13)$$

where $f(r)$, $\tilde{A}_t(r)$ and $h(r)$ are the background solutions. $u(r)$, $l(r)$, $a_0(r)$ and $\sigma(r)$ are the perturbations on the background. Then we obtain the linearized EoM as below,

$$\begin{aligned} \Delta u + (\omega - \tilde{g}\tilde{A}_t)^2 u - \gamma^2 u - 2(\omega - \tilde{g}\tilde{A}_t)\gamma l - 2\tilde{g}(\omega - \tilde{g}\tilde{A}_t)f a_0 - Uu - 2Su - Y\sigma &= 0 , \\ \Delta l + (\omega - \tilde{g}\tilde{A}_t)^2 l - \gamma^2 l + 2(\omega - \tilde{g}\tilde{A}_t)\gamma u - \tilde{g}\gamma f a_0 - Ul &= 0 , \\ \Delta a_0 - 2\tilde{g}^2 f^2 a_0 + 4\tilde{g}(\omega - \tilde{g}\tilde{A}_t)f u - 2\tilde{g}\gamma f l &= 0 , \\ \Delta \sigma - \gamma^2 \sigma - W\sigma - 2Yu &= 0 . \end{aligned} \quad (3.14)$$

where $\Delta = \sum_{i=1}^3 \partial_i \partial_i$ is the 3-dim Laplacian operator and

$$\begin{aligned} U(r) &= \left. \frac{\partial V}{\partial(\phi^* \phi)} \right|_{\phi^* \phi = f^2(r), h=h(r)} , \quad S(r) = \left. \frac{\partial^2 V}{\partial(\phi^* \phi)^2} \right|_{\phi^* \phi = f^2(r), h=h(r)} f^2(r) , \\ W(r) &= \left. \frac{1}{2} \frac{\partial^2 V}{\partial h^2} \right|_{\phi^* \phi = f^2(r), h=h(r)} , \quad Y(r) = \left. \frac{\partial^2 V}{\partial(\phi^* \phi) \partial h} \right|_{\phi^* \phi = f^2(r), h=h(r)} f(r) . \end{aligned} \quad (3.15)$$

The boundary conditions are

$$u'(0) = l'(0) = a'_0(0) = \sigma'(0) = 0, \quad u(\infty) = l(\infty) = a_0(\infty) = \sigma(\infty) = 0 . \quad (3.16)$$

We want to obtain the parameter γ of perturbations u, l, a_0, σ . The classically unstable mode correspond to $\gamma > 0$. We can do this by using the shooting method in Ref. [68]. We introduce four basis solutions $\Psi^{(i=1,2,3,4)}(r) = (u^{(i)}, l^{(i)}, a_0^{(i)}, \sigma^{(i)})$ which satisfy the Neumann boundary conditions $d\Psi^{(i)}/dr|_{r=0} = 0$ and Dirichlet boundary conditions $\Psi^{(1)}(0) = (1, 0, 0, 0)$, $\Psi^{(2)}(0) = (0, 1, 0, 0)$, $\Psi^{(3)}(0) = (0, 0, 1, 0)$ and $\Psi^{(4)}(0) = (0, 0, 0, 1)$. Then we integrate the Eqs. (3.14) numerically to find the values of $\Psi^{(i)}$ at large $r = r_\infty$. Now, recall that we are searching for a specific solution $\Psi(r) = c_1\Psi^{(1)}(r) + c_2\Psi^{(2)}(r) + c_3\Psi^{(3)}(r) + c_4\Psi^{(4)}(r)$ which satisfies $\Psi(r_\infty) = 0$. This gives the system of linear equations,

$$\hat{D}_c(c_1, c_2, c_3, c_4)^T = 0, \quad \hat{D}_c = (\Psi^{(1)T}, \Psi^{(2)T}, \Psi^{(3)T}, \Psi^{(4)T}). \quad (3.17)$$

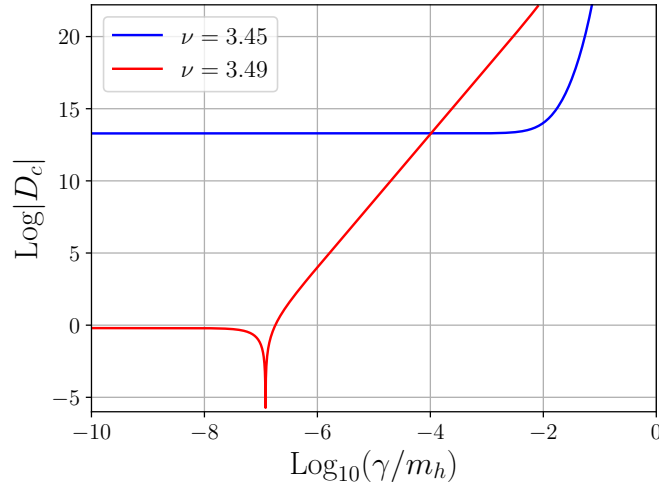


Figure 6. Determinant of matrix for $\nu = 3.45$ and $\nu = 3.49$ on the first branch respectively. We choose $\alpha^2 = 10^{-5}$, $k = 3.5$.

Equation (3.17) has nontrivial solutions only if $D_c \equiv \det \hat{D}_c = 0$. In figure 6 we plot $\text{Log}|D_c|$ as a function of $\text{Log}_{10}\gamma$ where we choose $\alpha^2 = 10^{-5}$ and $k = 3.5$. We found that there is no classically unstable mode for $\nu = 3.45$ as there is no solution for $\gamma > 0$. This also hold for other solutions of $U(1)$ gauged Q-balls except for $\nu \rightarrow k$ on the first branch. We found there is one unstable mode for $\nu = 3.49$. Actually, in the limit $\nu \rightarrow k$, the contribution of gauged field can be neglected and one expects that the case is similar to the non-gauged Q-ball where $\frac{dQ}{d\omega} > 0$ indicates there exists classically unstable mode. This is also discussed in Refs. [26, 64]. However, we usually do not have to worry about this because the region already has been excluded by the quantum instability. In Ref. [50], the authors have shown that the gauged Q-balls on the second branch with small gauge coupling are classically unstable with respect to axisymmetric perturbations. This enhances our confidence that the gauged Q-ball on the second branch is unstable. The region is almost covered by the stress stability criterion.

In summary, the parameter space of gauged Q-balls are shown in figure 7. The red line represents the region where the gauged Q-ball is dominated by the gauge field such that it

is unstable under stress stability criterion. The green line represents the region where the gauged Q-ball is unstable under quantum stability criterion. We only plot the quantum mechanical stability and the stress stability criterion because they cover the space which is classically unstable and is unstable against fission respectively. The gauged Q-ball is stable only in the region of $\nu \in [\nu_{\min}, \nu_{\max}]$. The ν_{\min} corresponds to the maximal charge of gauged Q-balls. In order to form a gauged Q-ball of given charge at given gauge coupling, the charge has to be smaller than the maximal charge. It should also be noted that, if the dark gauge boson of gauged Q-ball kinetically mixes with SM photons or Z bosons, this would produce distinct experimental signatures which can constrain Q-ball charge and couplings.

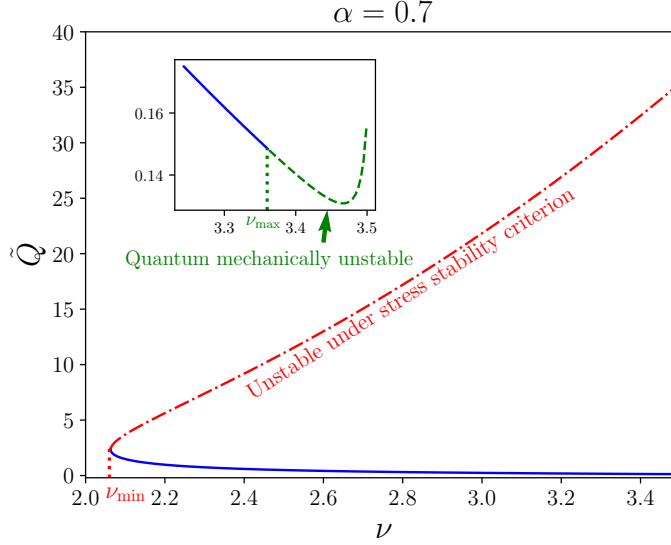


Figure 7. Viable space of ν of gauged Q-balls for $\alpha = 0.7$. The red line represents the region where the gauged Q-ball is dominated by gauge field such that it is unstable under stress stability criterion. The green line represents the region where the gauged Q-ball is unstable under quantum stability criterion. Gauged Q-balls in the blue region between ν_{\min} and ν_{\max} are stable.

4 Thin-wall approximation

As the radius of gauged Q-ball becomes large, the width of profile can be neglected and the gauged Q-balls can be depicted by the thin-wall approximation. The Higgs profile can be approximately viewed as a step function, the vacuum value is zero and v_0 inside and outside the Q-ball, respectively. The derivative of the Higgs field only contributes to the surface term of gauged Q-ball which is negligible when the radius of the ball is large. Then the problems are reduced to those or ones with two fields, ϕ and \tilde{A}_μ . We will discuss the simplified piecewise model and show that it behaves closely to the FLSM model. By using the mapping method introduced by Ref. [69], we give some semi-analytic results and some analytic evaluations of the maximal charge of gauged Q-balls.

4.1 Piecewise model

If the Higgs field is approximately $h(\rho) = v_0 \Theta(\rho - \rho_*)$, then we can approximately view the complex scalar moving in the piecewise parabolic potential [21, 70, 71]. The Lagrangian density can be further approximated as

$$\mathcal{L}_{\text{piecewise}} = (D_\mu \phi)^\dagger (D^\mu \phi) - \frac{1}{4} \tilde{A}_{\mu\nu} \tilde{A}^{\mu\nu} - m_\phi^2 \phi^\dagger \phi \Theta \left(1 - \frac{\phi^\dagger \phi}{v^2} \right) - m_\phi^2 v^2 \Theta \left(\frac{\phi^\dagger \phi}{v^2} - 1 \right) , \quad (4.1)$$

where $\Theta(x)$ is the Heaviside step function. In our case,

$$m_\phi = v_0 \sqrt{\frac{\lambda_{\phi h}}{2}}, \quad v = v_0 \sqrt{\frac{\lambda_h}{2\lambda_{\phi h}}} . \quad (4.2)$$

Note that v is chosen so that $V(\phi)$ is continuous at $\phi^\dagger \phi = v^2$. This can be understood from the EoM of the Higgs field in the FLSM model,

$$h''(r) + \frac{2}{r} h'(r) + \left[\frac{m_h^2}{2} - \lambda_h h(r)^2 - \lambda_{\phi h} f(r)^2 \right] h(r) = 0 , \quad (4.3)$$

where we use the definition $\phi(r, t) = f(r) e^{-i\omega t}$ and the prime denotes a derivative with respect to r . If the Higgs field is approximately a step function, we can neglect the derivatives, then we have

$$h^2 \approx \begin{cases} \frac{m_h^2}{2\lambda_h} - \frac{\lambda_{\phi h}}{\lambda_h} f^2 & \text{for } 2\lambda_{\phi h} f^2 < m_h^2 , \\ 0 & \text{for } 2\lambda_{\phi h} f^2 > m_h^2 , \end{cases} \quad (4.4)$$

and we could assume $f(r) \approx 0$ outside the bubble, for which $h^2 \approx \frac{m_h^2}{2\lambda_h} = v_0^2$. Therefore $V(\phi, h) \approx m_\phi^2 \phi^\dagger \phi$ outside the Q-ball and $V(\phi, h) \approx \frac{\lambda_h}{4} v_0^4$ inside the Q-ball. The consistency between the piecewise model and the Friedberg-Lee-Sirlin model has been discussed in Ref. [71] and the classical stability of gauged Q-balls in piecewise model has been studied in Ref. [64, 70]. The EoM of gauged Q-balls in the piecewise model after the rescaling of Eq. (2.19) are

$$\frac{1}{\rho^2} \partial_\rho (\rho^2 \partial_\rho \mathcal{A}) + (\nu - \alpha^2 \mathcal{A}) \Phi^2 = 0 , \quad (4.5)$$

$$\frac{1}{\rho^2} \partial_\rho (\rho^2 \partial_\rho \Phi) + [(\nu - \alpha^2 \mathcal{A})^2 - k^2 \Theta(1 - 4k^2 \Phi^2)] \Phi = 0 . \quad (4.6)$$

These equations are easier to solve than the FLSM model by using undershooting/overshooting method. The Q-ball energy and charge reads,

$$\tilde{E} = \frac{1}{k} \int_0^\infty d\rho \rho^2 \mathcal{E}, \quad \tilde{Q} = \int_0^\infty d\rho \rho^2 (\nu - \alpha^2 \mathcal{A}) \Phi^2 . \quad (4.7)$$

Here, $\mathcal{E} = \frac{\alpha^2}{2} (\partial_\rho \mathcal{A})^2 + \frac{1}{2} (\partial_\rho \Phi)^2 + \frac{1}{2} [(\nu - \alpha^2 \mathcal{A})^2 + k^2 \Theta(1 - 4k^2 \Phi^2)] \Phi^2 + \frac{1}{8} \Theta(4k^2 \Phi^2 - 1)$ which has a different form from the FLSM model.

We solve Eqs. (4.5) and (4.6) numerically to get the profiles of the complex field and the gauge field. Then we can get the charge and energy of gauged Q-balls by substituting them into Eqs. (4.7). These numerical results are shown in figure 8. We can see that the piecewise model fits the FLSM model well when the gauged Q-ball radius is large. The distinctions appear at small ρ_* at which the Higgs field value inside is not approximately zero.

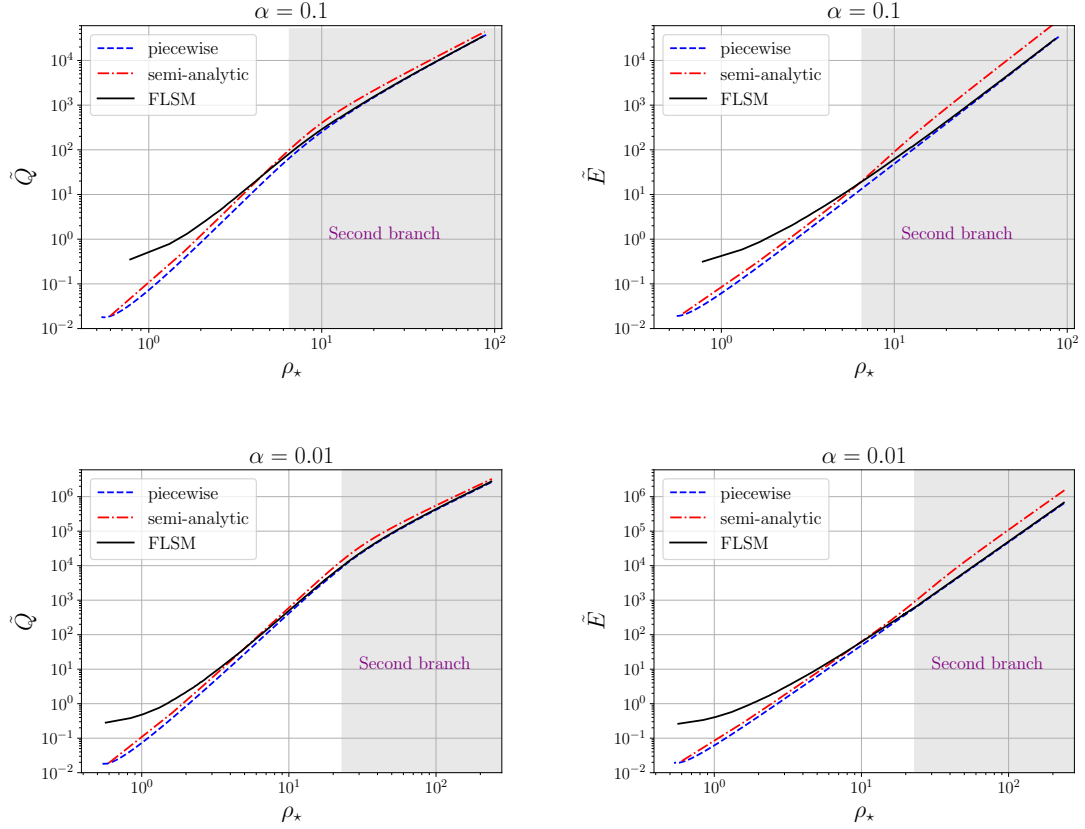


Figure 8. Charge and Energy as functions of Gauged Q-ball radius. The blue lines are the numerical results in piecewise model; red lines are the semi-analytic results Eq. (4.12) and Eq. (4.15), black lines come from the numerical results in FLSM model.

4.2 Mapping gauged Q-balls

We make a further assumption that the complex scalar field is also a step function, $\Phi(\rho) = \Phi_0(1 - \Theta(\rho - \rho_b))$, where we denote $\Phi_0 = \Phi(0)$ and ρ_b is defined by $\Phi(\rho_b) = \Phi_0/2$. Then the profile of gauged field is [23]

$$\mathcal{A}(\rho) = \frac{\nu}{\alpha^2} \begin{cases} 1 - \frac{\sinh(\alpha\Phi_0\rho)}{\cosh(\alpha\Phi_0\rho_b)\alpha\Phi_0\rho}, & \rho < \rho_b \\ \frac{\alpha\Phi_0\rho_b - \tanh(\alpha\Phi_0\rho_b)}{\alpha\Phi_0\rho}, & \rho > \rho_b \end{cases} \quad (4.8)$$

The Q-ball radius is defined by $\Phi(\rho_*) = \frac{1}{2k}$.

In Ref. [69], the authors propose a mapping between the gauged Q-ball and the global Q-ball. Specifically,

$$\nu = \nu_g \alpha \Phi_0 \rho_b \coth(\alpha \Phi_0 \rho_b), \quad (4.9)$$

where ν_g is the value of frequency for the global Q-ball with the same ρ_b . Then the profile of \mathcal{A} is given by Eq. (4.8). This relation holds even for cases beyond the thin-wall approximation. Interestingly, the global cases in the piecewise model have analytic

solutions [70]:

$$\Phi_g(\rho) = \begin{cases} \frac{1}{2k} \frac{\rho_\star \sin(\nu_g \rho)}{\rho \sin(\nu_g \rho_\star)}, & \rho < \rho_\star \\ \frac{1}{2k} \frac{\rho_\star e^{-\sqrt{k^2 - \nu_g^2} \rho}}{\rho e^{-\sqrt{k^2 - \nu_g^2} \rho_\star}}, & \rho > \rho_\star. \end{cases} \quad (4.10)$$

This gives us $\Phi_0 = \frac{1}{2k} \frac{\nu_g \rho_\star}{\sin(\nu_g \rho_\star)}$ and $2 \sin(\nu_g \rho_b) = \nu_g \rho_b$. Then we have $\nu_g \rho_b = C_1$ where $C_1 \approx 1.89549$ ². The Q-ball radius is defined as

$$\rho_\star(\nu_g) = \frac{1}{\nu_g} \left(\pi - \arctan \left(\frac{\nu_g}{\sqrt{k^2 - \nu_g^2}} \right) \right). \quad (4.11)$$

If we use $\Phi(\rho) = \Phi_0(1 - \Theta(\rho - \rho_b))$ and $\mathcal{A}(\rho)$ from Eq. (4.8), we have further semi-analytic results for charge:

$$\tilde{Q} = \frac{\nu_g \rho_b}{\alpha^2} (\alpha \Phi_0 \rho_b \coth(\alpha \Phi_0 \rho_b) - 1) = \frac{\rho_b}{\alpha^2} (\nu - \nu_g). \quad (4.12)$$

In the limit $\alpha \rightarrow 0$ and $\alpha \Phi_0 \rho_b \rightarrow 0$, because $x \coth x \sim 1 + \frac{x^2}{3} + \mathcal{O}(x^3)$ for $x \rightarrow 0$. Then we have $\tilde{Q} \sim \nu_g \Phi_0^2 \rho_b^3$. And in this case, when $\nu_g \rightarrow 0$, from Eq. (4.11) we have $\nu_g \rho_\star \simeq \pi$ and $\sin(\nu_g \rho_\star) \simeq \nu_g/k$, which lead to

$$\Phi_0 \simeq \frac{1}{2k} \frac{\pi}{\nu_g/k} = \frac{\pi}{2\nu_g}. \quad (4.13)$$

From $2 \sin(\nu_g \rho_b) = \nu_g \rho_b$, we have $\nu_g \sim \frac{C_1}{\rho_b}$, and

$$\tilde{Q} \propto \rho_b^4, \quad (4.14)$$

which is consistent with the global Q-ball case. Using the same procedure that derives Eq. (2.20), we have analytic results for total energy:

$$\begin{aligned} \tilde{E} &= \frac{\nu \tilde{Q}}{k} + \frac{1}{3k} \int d\rho \rho^2 \left[(\partial_\rho \Phi)^2 - \alpha^2 (\partial_\rho \mathcal{A})^2 \right] \\ &\simeq \frac{\nu \tilde{Q}}{k} + \frac{\Phi_0 \rho_b^2}{12k} - \frac{1}{3k} \frac{\nu^2 [\alpha \Phi_0 \rho_b (2 + \text{sech}^2(\alpha \Phi_0 \rho_b)) - 3 \tanh(\alpha \Phi_0 \rho_b)]}{2\alpha^3 \Phi_0}. \end{aligned} \quad (4.15)$$

The second term comes from the integration over discontinuous $(\partial_\rho \Phi)^2$ by using the approximation of energy conservation [72].

In the first limit of $\alpha \Phi_0 \rho_b \rightarrow 0$ and large ρ_b , the last term of Eq. (4.15) vanishes. We have $\nu \simeq \nu_g$, $\Phi_0 \simeq \frac{\pi}{2\nu_g} \simeq \frac{\rho_\star}{2}$ and $\rho_\star \simeq \rho_b$, then

$$\tilde{E} \simeq \frac{\pi \tilde{Q}}{k \rho_b} + \frac{\rho_b^3}{24k}, \quad (4.16)$$

which is just the energy of global Q-ball.

²The factor C_1 is close to the result of Ref. [46] where $C_1 \approx 2.08$ by using the definition $\Phi''(\rho_b) = 0$.

In the opposite limit $\alpha\Phi_0\rho_b \rightarrow \infty$, because $\mathcal{A} \rightarrow \tilde{Q}/\rho$, then from Eq. (4.8),

$$\nu = \frac{\alpha^2 \tilde{Q}}{\rho_b} \left(1 - \frac{\tanh(\alpha\Phi_0\rho_b)}{\alpha\Phi_0\rho_b} \right)^{-1} \simeq \frac{\alpha^2 \tilde{Q}}{\rho_b}. \quad (4.17)$$

Thus from Eq. (4.15) the energy of gauged Q-ball is

$$\tilde{E} \simeq \frac{\nu \tilde{Q}}{k} + \frac{\Phi_0 \rho_b^2}{12k} - \frac{1}{3k} \frac{\nu^2 \rho_b}{\alpha^2} \simeq \frac{2\alpha^2 \tilde{Q}^2}{3k\rho_b} + \frac{\Phi_0 \rho_b^2}{12k}. \quad (4.18)$$

The first term is the Coulomb energy and the second term is the potential energy difference between inside and outside of the Q-ball. The second term is proportional to ρ_b^2 because in this case the Compton wavelength of the gauge field $\frac{1}{g\nu_0\Phi_0}$ inside the Q-ball is much smaller than Q-ball radius, $r_b = \rho_b/m_h$. So the Q ball is superconducting. The potential energy is therefore zero inside as well as outside of the Q ball and is nonzero only in the shell around ρ_b [23].

For a given ρ_* , we can solve the Eq. (4.11) to get the corresponding ν_g . After using $\Phi_0 = \frac{1}{2k} \frac{\nu_g \rho_*}{\sin(\nu_g \rho_*)}$, $2\sin(\nu_g \rho_b) = \nu_g \rho_b$ and Eq. (4.9) we can get Φ_0 , ρ_b and ν of gauged Q-balls. Substitute them into Eqs. (4.12) and (4.15) to get the charge and energy of gauged Q-balls. These semi-analytic results are shown by the red lines in figure 8. We find the mapping works well for $\rho_* \gg 1$ on the first branch where the profiles of scalar fields ϕ and h can be safely viewed as step function. The semi-analytic results of energy doesn't work well for the second branch because the $\Phi_0 \neq \frac{1}{2k} \frac{\nu_g \rho_*}{\sin(\nu_g \rho_*)}$ which is the value in the global case. The value of Φ_0 is lower because the gauge potential dominates. This can be seen from figure 1. At the turning point between first branch and second branch, the discrepancy between semi-analytic results and numerical results is about a factor of $\mathcal{O}(1)$.

4.3 Maximal charge and energy of gauged Q-balls: analytic approximations

We give analytic evaluations of maximal charge and maximal energy of gauged Q-balls for a given gauge coupling. Because the gauged Q-balls should be unstable under stress stability criterion on the second branch where the gauge potential dominates, the maximal charge is approximately defined by $\left. \frac{d\nu}{d\rho_*} \right|_{\rho_*=\rho_{\max}} = 0$. In the limit at large Q-ball with $\nu_g \rightarrow 0$, we have $\rho_b = C_1/\nu_g$ and $\Phi_0 \simeq \frac{\rho_*}{2}$. Then, from (4.9) we get

$$\nu = \frac{C_1 \alpha \rho_*}{2} \coth \left(\frac{C_1 \alpha \rho_*}{2\nu_g} \right) = \frac{C_1 \alpha \rho_*}{2} \coth \left(\frac{C_1 \alpha \rho_*^2}{2\pi} \right), \quad (4.19)$$

where we used $\rho_* \simeq \pi/\nu_g$ when $\nu_g \rightarrow 0$. Then we have when the charge is maximal $\left. \frac{d\nu}{d\rho_*} \right|_{\rho_*=\rho_{\max}} = 0$,

$$\sinh \left(\frac{C_1 \alpha \rho_{\max}^2}{2\pi} \right) \cosh \left(\frac{C_1 \alpha \rho_{\max}^2}{2\pi} \right) = \frac{C_1 \alpha \rho_{\max}^2}{\pi}, \quad (4.20)$$

then we get $\frac{C_1 \alpha \rho_{\max}^2}{2\pi} = C_2$ with $C_2 \approx 1.08866$. So in this case $\alpha\Phi_0\rho_b \simeq C_2$ which is somewhere in the middle of Eq. (4.16) and Eq. (4.18). We can also get the minimal

frequency

$$\nu_{\min} = \frac{C_1 \alpha \rho_{\max}}{2} \coth \left(\frac{C_1 \alpha \rho_{\max}^2}{2\pi} \right) = \sqrt{\frac{\pi C_1 C_2 \alpha}{2}} \coth(C_2) \approx 2.26 \sqrt{\alpha}, \quad (4.21)$$

and the corresponding frequency for the global case $\nu_{g\min} = \frac{\pi}{\rho_{\max}} = \sqrt{\frac{\pi C_1 \alpha}{2 C_2}}$. We can see that $\frac{\nu_{\min}}{\nu_{g\min}} = C_2 \coth(C_2) \approx 1.367$ which is independent of the Q-ball size. This implies that as the solutions on the second branch are unstable, the gauged Q-ball lives on the first branch and is close to the global case.

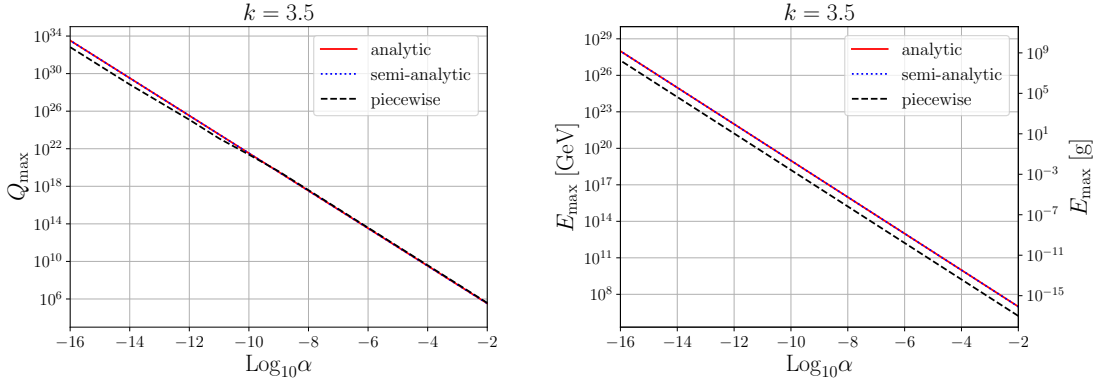


Figure 9. Maximal charge $Q_{\max} = \frac{2\pi}{\lambda_h} \tilde{Q}_{\max}$ (left panel) and energy $E_{\max} = \frac{2\pi m_\phi}{\lambda_h} \tilde{E}_{\max}$ (right panel) of gauged Q-ball for different α and k . The red lines are analytic evaluations Eq. (4.22) and (4.24); the blue dotted lines are the semi-analytic results and the black dashed lines represent the numerical results for piecewise model.

Finally, we get the maximal charge,

$$\tilde{Q}_{\max} = \frac{C_1}{\alpha^2} (C_2 \coth C_2 - 1) \approx 0.7 \alpha^{-2}, \quad (4.22)$$

from which we can see the charge is unbounded from above in the global case where $\alpha = 0$. The maximal energy reads

$$\begin{aligned} \tilde{E}_{\max} &= \frac{\nu_{\min} \tilde{Q}_{\max}}{k} + \frac{C_1^2 \rho_{\max}^3}{24\pi^2 k} - \frac{1}{3k} \frac{\nu_{\min}^2 [C_2(2 + \text{sech}^2 C_2) - 3 \tanh C_2]}{\alpha^3 \rho_{\max}} \\ &= \frac{\pi C_2 \coth C_2 \tilde{Q}_{\max}}{k \rho_{\max}} + \frac{C_1^2 \rho_{\max}^3}{24\pi^2 k} - \frac{1}{3k} \frac{\pi C_1 C_2 \coth^2 C_2 [C_2(2 + \text{sech}^2 C_2) - 3 \tanh C_2]}{2\alpha^2 \rho_{\max}}. \end{aligned} \quad (4.23)$$

By using $\nu_{\min} = \sqrt{\frac{\pi C_1 C_2 \alpha}{2}} \coth C_2$ and $\rho_{\max} = \sqrt{\frac{2\pi C_2}{C_1 \alpha}}$, we have

$$\begin{aligned} \tilde{E}_{\max} &= \frac{1}{k \alpha^{3/2}} \sqrt{\frac{\pi C_1 C_2}{72}} \left[-3C_1 \coth C_2 + C_2 \left(\frac{1}{\pi} + 4C_1 + 3C_1 \text{csch}^2 C_2 \right) \right] \\ &\approx 1.51 k^{-1} \alpha^{-3/2}. \end{aligned} \quad (4.24)$$

This also gives us $\tilde{E}_{\max} \propto \rho_{\max}^3 \propto \tilde{Q}_{\max}^{3/4}$ which is expected in the global case.

The analytic results of $Q_{\max} = \frac{2\pi}{\lambda_h} \tilde{Q}_{\max}$ and $E_{\max} = \frac{2\pi m_\phi}{\lambda_h} \tilde{E}_{\max}$ are shown in terms of the red lines in figure 9 and we can see that the maximal charge Q_{\max} fits well with the semi-analytic and numerical results. However, the analytic and semi-analytic E_{\max} is about 5-6 times larger than the numerical results due to the uncertainties of values of Φ_0 .

5 Gauged Q-ball DM from electroweak FOPT

In the above discussions, we have shown that the gauged Q-ball could be stable and hence can make a possible DM candidate. In this section, we begin to discuss the detailed production mechanism of the gauged Q-ball DM that is formed during the electroweak FOPT in the early Universe. We consider the minimal Higgs extended model with a singlet scalar field which could trigger a FOPT [47, 73, 74]. The phase transition dynamics can also be modified by introducing some new freedoms beyond the standard model.

5.1 Electroweak FOPT

The electroweak FOPT dynamics is determined by the finite temperature effective potential $V_{\text{eff}}(h, T)$ where h is the real component of the SM Higgs doublet as defined in Eq. (2.1),

$$V_{\text{eff}}(h, T) \equiv V_{\text{tree}}(h) + V_{\text{CW}}(h) + V_{\text{T}}(h, T) . \quad (5.1)$$

The first term $V_{\text{tree}}(h) = \lambda_h (h^2 - v_0^2)^2 / 4$ is the tree-level SM Higgs potential. $V_{\text{CW}}(h)$ is the one-loop quantum correction to the effective potential, i.e., Coleman-Weinberg potential. Using the on-shell renormalization scheme, we have

$$V_{\text{CW}}(h) = \sum_i (-1)^{F_i} \frac{g_i}{64\pi^2} \left[m_i^4(h) \left(\log \frac{m_i^2(h)}{m_i^2(v_0)} - \frac{3}{2} \right) + 2m_i^2(h)m_i^2(v_0) \right], \quad (5.2)$$

where g_i is the degree of freedom for each particle, $F_i = 1(0)$ for fermions(bosons), $m_i(h)$ are masses for t, W, Z, h, ϕ . The finite-temperature correction term is given by

$$V_{\text{T}}(h, T) = \sum_i (-1)^{F_i} \frac{g_i T^4}{2\pi^2} \int_0^\infty dx x^2 \log \left[1 \mp e^{\left(-\sqrt{x^2 + (m_i^2(h) + \Pi_i)/T^2} \right)} \right], \quad (5.3)$$

where the integral with “ $-/+$ ” sign denotes the contribution of bosons/fermions. Π_i is thermal masses of species i . Here, we use the daisy resummation scheme proposed by Dolan and Jackiw [75]. It is worth noticing that only the scalar fields and the longitudinal components of the gauge fields have nonzero Π_i . For the scalar fields

$$\Pi_h = \left(\frac{\lambda_h}{2} + \frac{\lambda_{\phi h}}{12} + \frac{3g^2 + g'^2}{16} + \frac{y_t^2}{4} \right) T^2, \quad \Pi_\phi = \frac{\lambda_{\phi h}}{6} T^2, \quad (5.4)$$

where g and g' are the gauge coupling of $SU(2)_L$ and $U(1)_Y$, respectively. For the longitudinal components of the gauge bosons, we have

$$\Pi_{W_L} = \Pi_{Z_L} = \frac{11g^2}{6} T^2, \quad \Pi_{B_L} = \frac{11g'^2}{6} T^2. \quad (5.5)$$

Hence, for the longitudinal components of the gauge bosons, their physical masses are eigenvalues of the following matrix

$$M_L^2 = \begin{pmatrix} m_1^2 + \Pi_{W_L} & 0 & 0 & 0 \\ 0 & m_1^2 + \Pi_{W_L} & 0 & 0 \\ 0 & 0 & m_1^2 + \Pi_{Z_L} & m_{12}^2 \\ 0 & 0 & m_{12}^2 & m_2^2 + \Pi_{B_L} \end{pmatrix}, \quad (5.6)$$

where $m_1^2 = g^2 h^2/4$, $m_2^2 = g'^2 h^2/4$ and $m_{12}^2 = -gg'h^2/4$.

Requiring the ordinary electroweak vacuum with $h = v_0 = 246$ GeV as the global vacuum at $T = 0$ or $V_{\text{eff}}(v_0, 0) < V_{\text{eff}}(0, 0)$ leads to

$$\lambda_{\phi h} \lesssim \frac{4\sqrt{2}\pi m_h}{v_0} \approx 9.0. \quad (5.7)$$

The phase transition is the process of symmetry breaking in the early Universe. Through a process of bubble nucleation, growth and merger, the Universe transits from a metastable state into a stable state. The critical temperature T_c is defined by the time when the two minima of effective potential is degenerate, $V_{\text{eff}}(v(T_c), T_c) = V_{\text{eff}}(0, T_c)$ with $v(T_c)$ being the vacuum value in the true vacuum at $T = T_c$. Bubbles begin to nucleate when the temperature drops to the nucleation temperature T_n . The nucleation rate of bubbles is given by

$$\Gamma(T) \approx T^4 \left(\frac{S_3(T)}{2\pi T} \right)^{3/2} e^{-S_3(T)/T}, \quad (5.8)$$

with $S_3(T)$ being the action of the $\mathcal{O}(3)$ symmetric bounce solution [76]. The nucleation temperature T_n is typically defined by

$$\Gamma(T_n) H^{-4}(T_n) \approx 1, \quad (5.9)$$

where $H(T)$ is the Hubble expansion rate,

$$H^2(T) = \frac{8\pi}{3M_{\text{pl}}^2} \left(\frac{\pi^2}{30} g_\star T^4 + \Delta V_{\text{eff}}(T) \right). \quad (5.10)$$

where $M_{\text{pl}} = 1.22 \times 10^{19}$ GeV is the Planck mass and g_\star is the number of relativistic degrees of freedom at temperature T . $\Delta V_{\text{eff}}(T)$ is the potential energy difference between false and true vacuum $\Delta V_{\text{eff}}(T) = V_{\text{eff}}(0, T) - V_{\text{eff}}(v(T), T)$. The potential difference between the inside and outside the bubbles will cause the bubbles expanding in the Universe so that the volume of the false vacuum diminishes with time. The probability of finding a point in the false vacuum reads,

$$p(T) = e^{-I(T)}, \quad (5.11)$$

where $I(T)$ is the fraction of vacuum converted to the true vacuum [77, 78],

$$I(T) = \frac{4\pi}{3} \int_T^{T_c} dT' \frac{\Gamma(T')}{T'^4 H(T')} \left[\int_T^{T'} d\tilde{T} \frac{v_w}{H(\tilde{T})} \right]^3. \quad (5.12)$$

In the radiation dominated Universe [78],

$$I(T) = \frac{675 M_{\text{pl}}^4}{4\pi^5 g_\star^2} \int_T^{T_c} \frac{dT' \Gamma(T')}{T'^6} \left(\frac{1}{T} - \frac{1}{T'} \right)^3. \quad (5.13)$$

The percolation temperature T_p , is defined by $I(T_p) = 0.34$ [77]. This means that 34% of the false vacuum has been converted to the true vacuum at T_p . The percolation temperature T_p is also the temperature at which the GW is produced from the FOPT [78–82].

We use the following definition of the phase transition strength:

$$\alpha(T) \equiv \frac{\left(1 - \frac{T}{4} \frac{\partial}{\partial T}\right) \Delta V_{\text{eff}}}{\rho_r}, \quad (5.14)$$

where $\rho_r = \pi^2 g_\star T^4/30$ represents radiation energy density and ΔV_{eff} is the potential difference between the false and the true vacua. The inverse time duration β at fixed temperature T_i is defined as

$$\beta = H(T) T \frac{d}{dT} \left(\frac{S_3}{T} \right) \Big|_{T=T_i}. \quad (5.15)$$

We use CosmoTransitions [83] to calculate the phase transition dynamics. In the left panel of figure 10, we show the three typical temperatures of the FOPT process in the minimal SM plus singlet model. And in the right panel of figure 10, we show the wash-out parameter $v(T)/T$ at these different temperatures.

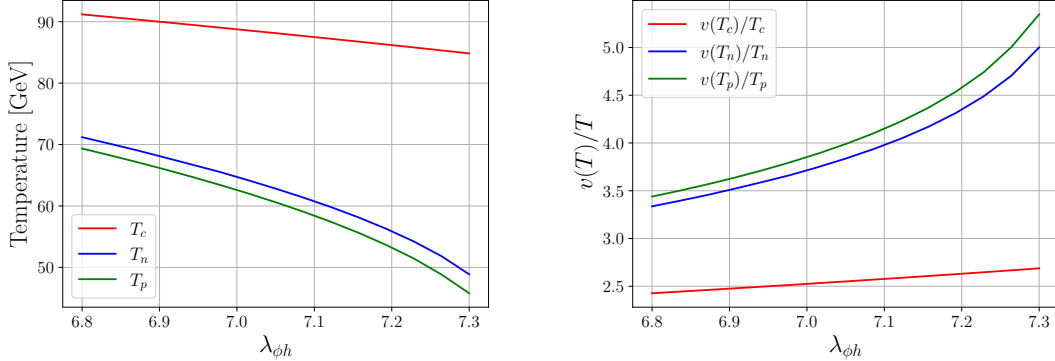


Figure 10. Phase transition parameters as functions of $\lambda_{\phi h}$. Left: the critical, nucleation and percolation temperatures for different values of $\lambda_{\phi h}$. For the percolation temperature we choose $v_w = 0.1$. Right: the wash-out parameters $v(T)/T$ for various temperatures as functions of $\lambda_{\phi h}$.

5.2 Bubble wall filtering during FOPT

As the particles gain mass inside the bubble, due to the energy conservation, only high-energy particles can pass through the bubbles walls and the others are reflected. The condition of penetration in the bubble wall frame reads [19, 20]:

$$p_z^w > \sqrt{\Delta m_i^2}, \quad (5.16)$$

where p_z^w is the particle z -direction momentum in the bubble wall frame, $\Delta m_i^2 = (m_i^{\text{in}})^2 - (m_i^{\text{out}})^2$ is the mass difference between the true and false vacuum where m_i^{in} is the particle mass in the true vacuum and m_i^{out} is the mass in the false vacuum [84] which we will set to zero in this work.

The particle flux coming from the false vacuum per unit area and unit time can be written as [19, 20]

$$J_i^w = g_i \int \frac{d^3 p^w}{(2\pi)^3} \frac{p_z^w}{\sqrt{(p^w)^2 + (m_i^{\text{out}})^2}} f_i^{\text{eq}} \Theta(p_z^w - \sqrt{\Delta m^2}) , \quad (5.17)$$

where g_i is degrees of freedom of the particle. p^w is the magnitude of the three-momentum of the particles. f_i^{eq} is the equilibrium distribution outside the bubble in the bubble wall frame,

$$f_i^{\text{eq}} = \frac{1}{e^{\gamma_w (\sqrt{(p^w)^2 + (m_i^{\text{out}})^2} - v_w p_z^w)/T} \mp 1} , \quad (5.18)$$

where \mp is for bosons and fermions respectively. v_w is the bubble wall velocity and $\gamma_w = 1/\sqrt{1 - v_w^2}$ is its Lorentz boost factor. The particle number density inside the bubble n_i^{in} in the bubble center frame can be written as

$$n_i^{\text{in}} = \frac{J_i^w}{\gamma_w v_w} . \quad (5.19)$$

Assuming the particles are massless in the false vacuum, we can integrate Eq. (5.17) analytically and get [20, 85]

$$n_i^{\text{in}} \simeq \frac{g_i T^3}{\gamma_w v_w} \left(\frac{\gamma_w (1 - v_w) m_i^{\text{in}}/T + 1}{4\pi^2 \gamma_w^3 (1 - v_w)^2} \right) e^{-\frac{\gamma_w (1 - v_w) m_i^{\text{in}}}{T}} , \quad (5.20)$$

where we have used Maxwell-Boltzmann approximation of DM distribution. One can see that as $v_w \rightarrow 1$, Eq. (5.20) approaches $n_i^{\text{out}} = g_i T^3/\pi^2$, which is approximately the equilibrium number density for Boltzmann distribution outside the bubble. The fraction of particles i that are trapped into the false vacuum is defined by

$$F_i^{\text{trap}} = 1 - \frac{n_i^{\text{in}}}{n_i^{\text{out}}} . \quad (5.21)$$

In our case, complex scalars ϕ and ϕ^\dagger are trapped into the false vacuum due to the filtering effect. The symmetric part would annihilate away in terms of the process $\phi + \phi^\dagger \rightarrow h + h$, then the asymmetric part survives and composes the charge of gauged Q-balls. It can be easily seen that the penetrated particle number density is sensitive to the bubble wall velocity as it appears in the exponent of Eq. (5.20). The precise calculation of bubble wall velocity [86–93] is beyond the scope of this work and we set it as a free parameter.

5.3 Charge of Q-ball in the electroweak FOPT

We can define T_\star as the temperature at which the false vacuum or old phase remnants can still form an infinitely connected “cluster”, just like the definition of percolation temperature [17]. The T_\star satisfies $p(T_\star) = 1 - p(T_p) = 0.29$ which corresponds to $I(T_\star) = 1.24$. T_\star

is the temperature when Q-balls start to form. Below the temperature T_* , the false vacuum remnants formed during FOPT may further fragment into smaller pieces. Ultimately, these pieces would shrink into Q-balls if there exists a non-zero primordial charge asymmetry. We can define the critical radius, r_c , at which the remnant shrinks to an insignificant size before another true vacuum bubble form within it [14]. This means [17]

$$\Gamma(T_*) \left(\frac{4\pi}{3} r_c^3 \right) \Delta t \sim 1. \quad (5.22)$$

where $\Delta t = r_c/v_w$ is the time cost for shrinking. The number density of the remnants n_Q^* can be expressed as:

$$n_Q^* \simeq 0.29 \left(\frac{3}{4\pi} \right)^{1/4} \left(\frac{\Gamma(T_*)}{v_w} \right)^{3/4}, \quad (5.23)$$

since the condition $n_Q^* \left(\frac{4\pi}{3} r_c^3 \right) = p(T_*) \simeq 0.29$.

The formation of Q-balls requires a nonzero conserved primordial charge which comes from the primordial DM asymmetry $\eta_\phi = (n_\phi - n_{\phi^\dagger})/s$. The entropy density $s = 2\pi^2 g_* T^3/45$. If the DM asymmetry is produced by thermal freeze-out in the early Universe, it is bounded from above by the equilibrium value,

$$\eta_\phi \lesssim \eta_\phi^{\text{eq}} = \frac{n_\phi^{\text{eq}}(T)}{s(T)} \simeq 5.1 \times 10^{-3} \times \left(\frac{108.75}{g_*} \right), \quad (5.24)$$

where we have used $n_\phi^{\text{eq}}(T) = 2\zeta(3)T^3/\pi^2$ with $\zeta(3) = 1.20206$ being the value of Riemann zeta function $\zeta(s)$ at $s = 3$. In order to overcome this constraint, we assume the DM is produced by some non-thermal processes like decay. In this work, we do not specify the origin of primordial charge of the complex scalar ϕ . In the early Universe at higher temperature, new physical processes beyond the standard model may have occurred. The would-be Q-ball DM particles ϕ may have their own conserved charge and be created in asymmetric decays of heavier particles [94]. For example, heavy Majorana neutrino could decay into a light fermion and a scalar, like $N \rightarrow \bar{\chi} + \phi$ and $N \rightarrow \chi + \phi^\dagger$ where χ is a fermion [95]. Assuming the process is CP-violating, the decay rates of these two channels differentiate from each other at loop level (when the ϕ is the standard model Higgs and χ is leptons, this is the process of leptogenesis.). So the asymmetry between ϕ and ϕ^\dagger appears and is retained until the phase transition in this work. The large DM asymmetry can be discussed in a similar manner to the large lepton asymmetry in the leptogenesis scenarios. Recent measurement of ^4He abundance coming from the EMPRESS experiment suggests a large degeneracy parameter of the electron neutrino [96],

$$\xi_e = 0.05_{-0.02}^{+0.03}. \quad (5.25)$$

Since the neutrino oscillations among three flavors, the neutrinos with three flavors have the same amount of asymmetry, and then the total lepton asymmetry reads,

$$\eta_L \equiv 3 \frac{n_{\nu_e} - n_{\bar{\nu}_e}}{s} = 3 \frac{T^3 \xi_e/6}{2\pi^2 g_{BBN} T^3/45} \simeq 5.3 \times 10^{-3}, \quad (5.26)$$

where $g_{BBN} = 10.75$ is the relativistic degree of freedom at the epoch of big bang nucleosynthesis. The large lepton asymmetry may come from the low scale leptogenesis [97, 98], Affleck-Dine mechanism [99] or L-ball decay [100].

In a remnant, the trapped Q-charge is given by $Q_\star = F_\phi^{\text{trap}} \eta_\phi s_\star / n_Q^\star$. In figure 11, we show the charge of the gauged Q-ball DM formed during the FOPT for different values of bubble wall velocities. We have chosen $\eta_\phi = \eta_L$. When $\lambda_{\phi h}$ is larger, both the $\Gamma(T_\star)$ and the Q-ball number density are suppressed, so that the charge is larger at a given η_ϕ .

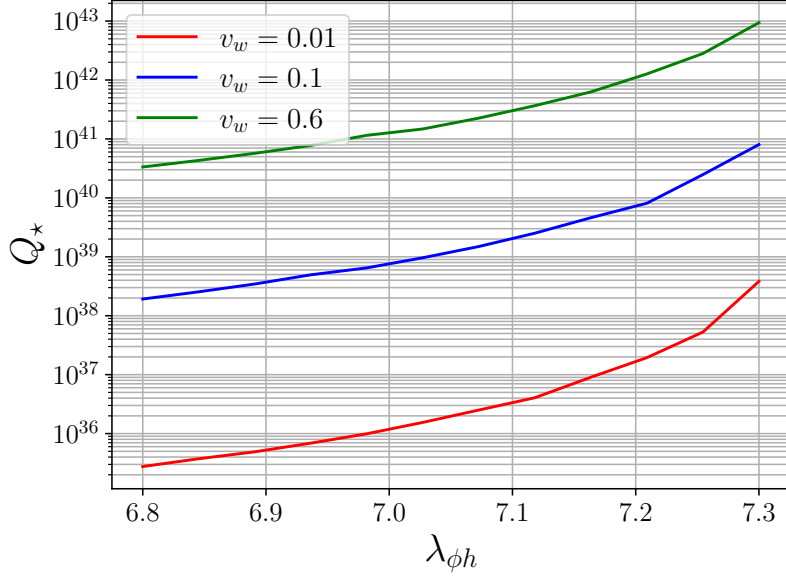


Figure 11. Charge of gauged Q-ball in electroweak FOPT. Here we choose $\eta_\phi = \eta_L$.

Since n_Q/s and Q does not change in the adiabatic Universe, at present they are

$$n_Q = \frac{n_Q^\star}{s_\star} s_0, \quad Q = Q_\star, \quad (5.27)$$

with $s_0 = 2891.2 \text{ cm}^{-3}$ being the entropy density in current time [101].

We take the approximation $T_\star \approx T_p$ then the bounce action can be approximated written as [102]

$$\frac{S_3(T_\star)}{T_\star} \simeq 131 - 4 \ln \left(\frac{T_\star}{100 \text{ GeV}} \right) - 4 \ln \left(\frac{\beta/H_\star}{100} \right) + 3 \ln v_w - 2 \ln \left(\frac{g_\star}{100} \right), \quad (5.28)$$

where $\beta/H_\star = \beta/H|_{T=T_\star}$. By approximately using $\Gamma(T_\star) \approx T_\star^4 e^{-S_3(T_\star)/T_\star}$, then we get

$$Q = 5.35 \times 10^{36} F_\phi^{\text{trap}} \left(\frac{v_w}{0.01} \right)^3 \left(\frac{\eta_\phi}{\eta_L} \right) \left(\frac{100 \text{ GeV}}{T_\star} \right)^3 \left(\frac{100}{\beta/H_\star} \right)^3 \left(\frac{100}{g_\star} \right)^{1/2}. \quad (5.29)$$

In order to get stable gauged Q-ball with a given value of charge, we must impose $Q_{\max} > Q$, so the gauge coupling \tilde{g} has to satisfy

$$\tilde{g} < 1.28 \times 10^{-18} \left(\frac{1}{F_{\phi}^{\text{trap}}} \right)^{1/2} \left(\frac{0.01}{v_w} \right)^{3/2} \left(\frac{\eta_L}{\eta_{\phi}} \right)^{1/2} \left(\frac{T_{\star}}{100 \text{ GeV}} \right)^{3/2} \left(\frac{\beta/H_{\star}}{100} \right)^{3/2} \left(\frac{g_{\star}}{100} \right)^{1/4}. \quad (5.30)$$

5.4 Relic density of gauged Q-ball DM

The DM relic density can also have the contribution from the standard freeze-out, through the process $\phi + \phi^{\dagger} \leftrightarrow h + h$. The relic abundance reads,

$$\Omega_{\text{freeze-out}} h_{100}^2 \approx \frac{2.58 \times 10^{-10} \text{ GeV}^{-2}}{\langle \sigma_{\text{anni}} v_{\text{rel}} \rangle}, \quad (5.31)$$

where $\langle \sigma_{\text{anni}} v_{\text{rel}} \rangle$ is the annihilation cross section. $h_{100} = H_0 / (100 \text{ km} \cdot \text{s}^{-1} \cdot \text{Mpc}^{-1}) = 0.67$ where H_0 is the Hubble constant today [103]. The cross section of process $\phi + \phi^{\dagger} \leftrightarrow h + h$ reads $\frac{\lambda_{\phi h}^2}{64\pi m_{\phi}^2} \left(1 - \frac{m_h^2}{m_{\phi}^2} \right)^{1/2}$ [104]. In our parameter space, where the $\lambda_{\phi h}$ is around 7, the relic abundance from freeze-out is approximately $\Omega_{\text{freeze-out}} h_{100}^2 \approx 2.35 \times 10^{-4}$. So we can omit the DM produced from thermal freeze-out.

The DM relic density also receives the contribution from penetrated asymmetric components of DM particles which is given by the excess of ϕ over ϕ^{\dagger} ,

$$\Omega_{\text{asymmetric}} h_{100}^2 = (1 - F_{\phi}^{\text{trap}}) \eta_{\phi} s_0 m_{\phi}. \quad (5.32)$$

The relic density of Q-balls at present is

$$\Omega_Q h_{100}^2 = \frac{n_Q E_Q}{\rho_c} h_{100}^2, \quad (5.33)$$

where $\rho_c = 3H_0^2 M_{\text{pl}}^2 / (8\pi)$ is the critical energy density. We have found that, the gauged Q-ball is generally a mixed state of Eq. (4.16) and Eq. (4.18) as $0 \leq \alpha B_0 \rho_b \leq C_2$. So we can write down the energy of gauged Q-ball at a given charge,

$$E_Q \simeq \frac{\pi Q}{r_{\star}} + \frac{4\pi}{3} r_{\star}^3 V_0 + \frac{3}{20\pi} \frac{\tilde{g}^2 Q^2}{r_{\star}}, \quad (5.34)$$

where $V_0 = \frac{\lambda_h}{4} v_0^4$ is the potential difference between inside and outside of the gauged Q-balls at zero temperature. The first term on the right-side is the zero-point energy of the scalar particles, the second term is the vacuum volume energy inside the Q-ball and the third term is the electrostatic self energy. By minimizing this expression respect to r_{\star} , we obtain,

$$E_Q = \frac{4\pi}{3} (4V_0)^{1/4} Q^{3/4} \left(1 + \frac{3\tilde{g}^2 Q}{20\pi^2} \right)^{3/4}. \quad (5.35)$$

We can see that in the limit of zero gauge coupling

$$E_Q = \frac{4\pi}{3} (4V_0)^{1/4} Q^{3/4} = \frac{4\pi}{3} Q^{3/4} \lambda_h^{1/4} v_0, \quad (5.36)$$

which is just the energy of global Q-ball. By using $n_Q = n_Q^* s_0/s_*$ and $Q = Q_* = F_\phi^{\text{trap}} \eta_\phi s_*/n_Q^*$, we finally arrive at the expression:

$$\begin{aligned} \Omega_Q h_{100}^2 & \simeq 2.81 \times \left(\frac{s_0 h_{100}^2}{\rho_c} \right) \left(\frac{\Gamma(T_*)}{v_w} \right)^{3/16} s_*^{-1/4} (F_\phi^{\text{trap}} \eta_\phi)^{3/4} \lambda_h^{1/4} v_0 \left(1 + \frac{108^{1/4} \tilde{g}^2 F_\phi^{\text{trap}} \eta_\phi s_* v_w^{3/4}}{5.4 \pi^{7/4} \Gamma(T_*)^{3/4}} \right), \end{aligned} \quad (5.37)$$

the $\Gamma(T_*)$ can also be expanded by using $\Gamma(T_*) \approx T_*^4 e^{-S_3(T_*)/T_*}$ and Eq. (5.28), but we keep the expression here to give more accurate results.

Although the expression hitherto is general, we apply these to the minimal SM plus singlet model. We choose $\lambda_{\phi h} = 6.8$ for which $T_n = 71.65$ GeV and $T_p = 68.9$ GeV. The number density of gauged Q-balls at production is $n_Q^* \simeq 3.0 \times 10^{-31} \text{ GeV}^{-3}$. In this case, the value of $v(T_p)/T_p$ is approximately 3.5 and there are still 50% of the DM particles trapping inside the false vacuum even at $v_w = 0.6$. But it should be noted that in this case, the contribution from penetrated asymmetric DM will dominate, as can be seen in Eq. (5.32). This can be avoided in two ways. One way is to increase the phase transition strength and the corresponding $v(T)/T$ so there are little DM particles penetrating into the true vacuum, resulting $F_\phi^{\text{trap}} \approx 1$. This can be achieved by introducing new freedoms beyond the standard model or considering dark FOPT instead of electroweak FOPT. The other way is model dependent: one can introduce new decay channels that penetrated ϕ could decay into dark radiation or SM leptons which can account for the lepton asymmetry. The decay process does not destroy the stability of Q-balls as long as $\pi/r_* < m_d$ where m_d is the mass of decay products. In this work we focus on the gauged Q-ball DM so we do not consider the penetrated asymmetric DM in details.

A strong FOPT requires large portal coupling $\lambda_{\phi h} = 6.8$, and the validity of the perturbative analysis should be roughly smaller than 10 [105]. The condition of a strong FOPT leads to large deviation of triple Higgs coupling, which might be detected by the loop-induced $e^+e^- \rightarrow hZ$ process [106, 107] at future lepton colliders, such as FCC-ee, CEPC, and ILC.

We show the gauged Q-ball DM relic density in figure 12. The colored star represents the value for the gauged Q-ball with maximal charge. The gray region represents the region where the DM is overproduced. We can see that due to the finiteness of the charge of gauged Q-balls, the gauged Q-balls can explain the whole DM at $v_w = 0.01$ only when the rescaled gauge coupling $\alpha \lesssim 10^{-16}$. The DM relic density is slightly enhanced due to the extra electrostatic energy.

In table 1 we choose four benchmark points that satisfy the correct DM relic density and show the corresponding F_ϕ^{trap} and η_ϕ/η_L . Besides, we also show the fractional change in Zh production relative to the SM prediction at one loop, $\delta\sigma_{Zh}$. We can see that the value of the required DM asymmetry η_ϕ is close to the lepton asymmetry η_L . This prompts us to speculate that they have the same origin. Actually, if the DM asymmetry comes from the process $N \rightarrow \bar{\chi} + \phi$ and $N \rightarrow \chi + \phi^\dagger$. We could assume the dark fermion χ is long-lived and decay suddenly into leptons after electroweak phase transition in order to avoid the

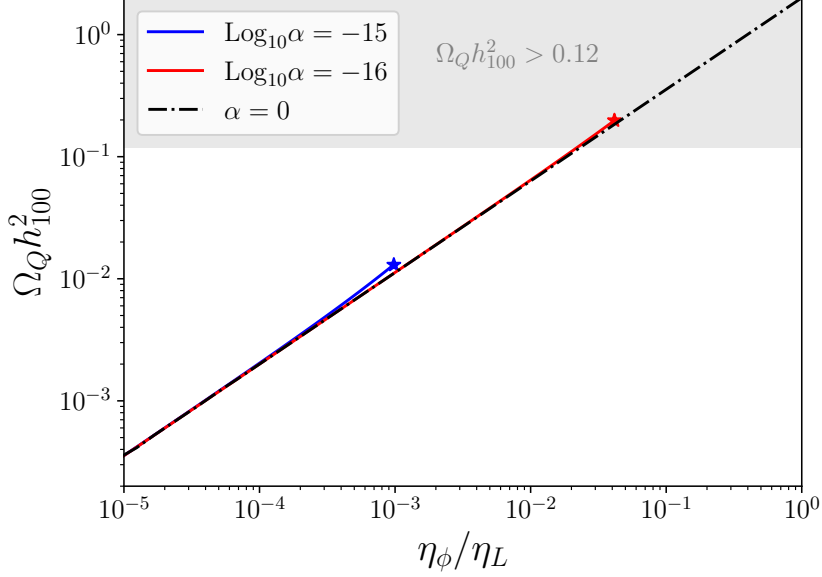


Figure 12. Q-ball relic density as function of DM asymmetry η_ϕ/η_L in the SM plus singlet model where $\lambda_{\phi h} = 6.8$. We choose $v_w = 0.01$. The star represents the value for the gauged Q-ball with maximal charge. The gray region represents the region where the DM is overproduced.

	$\lambda_{\phi h}$	T_p [GeV]	α_p	β/H_p	v_w	F_ϕ^{trap}	η_ϕ/η_L	$\delta\sigma_{Zh}$	GW
BP_1	6.8	69.8	0.12	540	0.1	0.932	0.48	-0.36%	●
BP_2	6.8	70.4	0.12	578	0.6	0.805	3.0	-0.36%	●
BP_3	7.0	63.0	0.15	372	0.1	0.965	3.4	-0.37%	●
BP_4	7.0	63.9	0.15	403	0.6	0.858	20.8	-0.37%	●

Table 1. Parameters of the model and phase transitions that satisfy $\Omega_Q h_{100}^2 \equiv 0.12$. We choose $\alpha = \tilde{g}/\sqrt{2\lambda_h} = 10^{-18}$. F_ϕ^{trap} is the fraction of DM particles which are trapped inside the false vacuum and η_ϕ/η_L is the DM asymmetry compared with the lepton asymmetry. $\delta\sigma_{Zh}$ is the fractional change in Zh production relative to the SM prediction at one loop. GW represents the corresponding GW spectra in figure 14.

electroweak sphaleron process. Then we expect the η_ϕ and η_L is at the same order. The detailed model building is beyond the scope of this work and we leave this in our future studies.

6 Constraints and detection of gauged Q-ball DM

6.1 Direct detection and astronomical constraints

We keep the gauged Q-ball DM mass and radius as free parameters to discuss its detection potential or constraints. The variation of gauged Q-ball DM mass and radius can be easily realize by varying the primordial DM asymmetry or the phase transition dynamics. The

combined constraints of gauged Q-ball are shown in figure 13. As we have discussed in the previous sections, the size of the gauged Q-ball is restricted to be finite. The maximal charges or the maximal mass of gauged Q-ball DM at given gauge coupling are marked by the stars in figure 13. The gray region denotes the constraints from cosmic microwave background (CMB) which is affected by DM-baryon scattering [108, 109]. DM cross sections have been probed by a variety of shallow and deep underground DM or repurposed experiments: XENON1T (orange) [110, 111], Mica (purple) [112, 113], Ohya (green) [114]. The Q-ball DM would transfer energy with other objects primarily through elastic scattering, approximately utilizing their geometric cross-section. When these cross-sections are sufficiently large, the resultant linear energy transfer might trigger observable phenomena. For example, if a macroscopic DM traverses compact objects such as white dwarfs or neutron stars and triggers thermonuclear runaway, this could potentially lead to a type IA supernova or superburst, respectively [115]. The brown region represents constraints from superbursts in neutron stars [116] and the blue region from white dwarf becoming supernovae [115, 116]. Combined all constraints in figure 13, one can see that the gauged Q-balls could be the DM candidate in a wide region of parameter space.

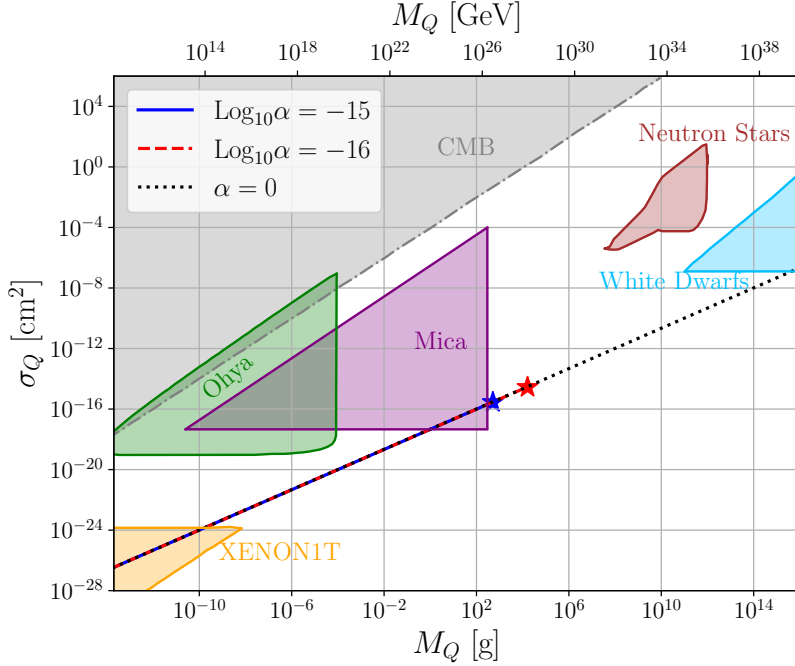


Figure 13. Combined constraints of direct detection and astronomical experiments on gauged Q-ball DM in the SM plus singlet model where $\lambda_{\phi h} = 6.8$. The value corresponding to maximal charge is marked by a star.

6.2 Phase transition GW

The phase transition GW spectra comes from three sources of a strong FOPT: bubble collision, sound wave, and turbulence.

- Bubble collision

The formula of phase transition GW from bubble collisions [117, 118] at the percolation temperature T_p , reads:

$$\Omega_{\text{co}} h_{100}^2 \simeq 1.67 \times 10^{-5} \left(\frac{H_p}{\beta} \right)^2 \left(\frac{\kappa_h \alpha_p}{1 + \alpha_p} \right)^2 \left(\frac{100}{g_\star} \right)^{1/3} \frac{0.11 v_w^3}{0.42 + v_w^2} \frac{3.8 (f/f_{\text{co}})^{2.8}}{1 + 2.8 (f/f_{\text{co}})^{3.8}}, \quad (6.1)$$

where β/H_p and α_p are defined at percolation temperature, respectively. κ_h represents the fraction of vacuum energy converted into the scalar field's gradient energy. f_{co} is the peak frequency of bubble collision:

$$f_{\text{co}} \simeq 1.65 \times 10^{-5} \text{ Hz} \left(\frac{\beta}{H_p} \right) \left(\frac{0.62}{1.8 - 0.1 v_w + v_w^2} \right) \left(\frac{T_p}{100 \text{ GeV}} \right) \left(\frac{g_\star}{100} \right)^{1/6}. \quad (6.2)$$

- Sound wave

The contribution from sound waves could be more significant. The formula GW spectrum from sound waves is [119]:

$$\Omega_{\text{sw}} h_{100}^2 \simeq 2.65 \times 10^{-6} \Upsilon_{\text{sw}} \left(\frac{H_p}{\beta} \right) \left(\frac{\kappa_v \alpha_p}{1 + \alpha_p} \right)^2 \left(\frac{100}{g_\star} \right)^{1/3} v_w (f/f_{\text{sw}})^3 \left(\frac{7}{4 + 3 (f/f_{\text{sw}})^2} \right)^{7/2}, \quad (6.3)$$

where κ_v reflects the fraction of vacuum energy that transfers into the fluid's bulk motion. The peak frequency of sound waves processes is:

$$f_{\text{sw}} \simeq 1.9 \times 10^{-5} \text{ Hz} \frac{1}{v_w} \left(\frac{\beta}{H_p} \right) \left(\frac{T_p}{100 \text{ GeV}} \right) \left(\frac{g_\star}{100} \right)^{1/6}. \quad (6.4)$$

Υ_{sw} is the suppression factor of the short period of the sound wave,

$$\Upsilon_{\text{sw}} = \left(1 - \frac{1}{\sqrt{1 + 2\tau_{\text{sw}} H_p}} \right), \quad (6.5)$$

where

$$\tau_{\text{sw}} H_p \approx (8\pi)^{1/3} \frac{v_w (H_p/\beta)}{\sqrt{3\kappa_v \alpha_p / (4 + 4\alpha_p)}}. \quad (6.6)$$

- Turbulence

The formula of the GW spectrum from turbulence is [120]:

$$\Omega_{\text{turb}} h_{100}^2 \simeq 3.35 \times 10^{-4} \left(\frac{H_p v_w}{\beta} \right) \left(\frac{\kappa_{\text{turb}} \alpha_p}{1 + \alpha_p} \right)^{3/2} \left(\frac{100}{g_\star} \right)^{1/3} \frac{(f/f_{\text{turb}})^3}{(1 + f/f_{\text{turb}})^{11/3} (1 + 8\pi f/H_p)}, \quad (6.7)$$

note that H_p is the Hubble rate at T_p :

$$H_p = 1.65 \times 10^{-5} \text{ Hz} \left(\frac{T_p}{100 \text{ GeV}} \right) \left(\frac{g_\star}{100} \right)^{1/6}, \quad (6.8)$$

and the peak frequency of turbulence processes is :

$$f_{\text{turb}} \simeq 2.7 \times 10^{-5} \text{ Hz} \frac{1}{v_w} \left(\frac{\beta}{H_p} \right) \left(\frac{T_p}{100 \text{ GeV}} \right) \left(\frac{g_\star}{100} \right)^{1/6}. \quad (6.9)$$

κ_{turb} represents the efficiency of vacuum energy being converted into turbulent flow:

$$\kappa_{\text{turb}} = \tilde{\epsilon} \kappa_v , \quad (6.10)$$

where the $\tilde{\epsilon}$ is set to 0.1.

The total contribution to the GW spectra can be calculated by summing these individual contributions:

$$\Omega_{\text{GW}} h_{100}^2 = \Omega_{\text{co}} h_{100}^2 + \Omega_{\text{sw}} h_{100}^2 + \Omega_{\text{turb}} h_{100}^2 . \quad (6.11)$$

We show the GW spectra $\Omega_{\text{GW}} h_{100}^2$ for four benchmark points in figure 14. These four benchmark points are shown in Table 1. We choose $\lambda_{\phi h} = 6.8$ and 7.0 and for each value of $\lambda_{\phi h}$ we choose two bubble wall velocities $v_w = 0.1, 0.6$. The colored regions represent the sensitivity curves for future GW detectors LISA [39] and TianQin [40, 41] with the signal-to-noise ratio (SNR) about 5. We can see that the LISA and TianQin could detect this new DM mechanism when the bubble wall velocity is relatively large. Taiji [42], BBO [43], DECIGO [44], Ultimate-DECIGO [45] could also detect this new DM mechanism by GW signals.

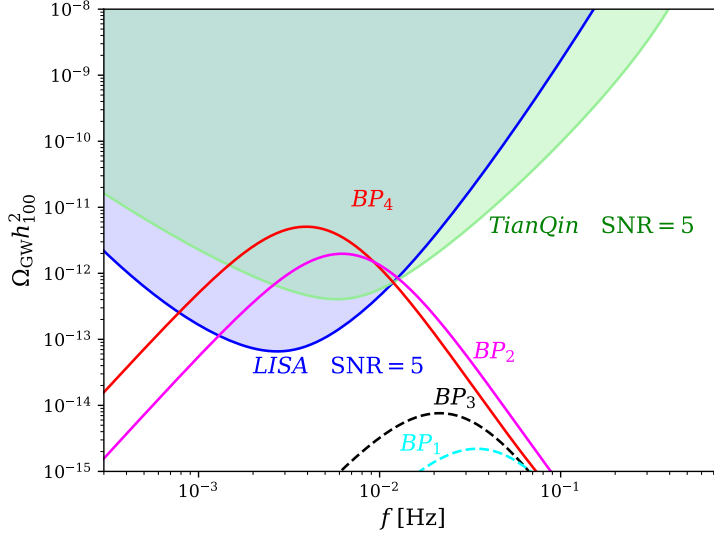


Figure 14. GW spectra for four benchmark points in Table 1. The future GW detectors LISA [39], TianQin [40, 41] could detect BP_2 and BP_4 whose bubble wall velocities are relatively large.

7 Discussion and conclusion

In this work, we have systematically discussed the gauged Q-ball DM formed during a FOPT. We have investigated the stability of gauged Q-balls, including quantum stability, stress stability, fission stability, and classical stability. Different from the global Q-balls, the gauge interaction restricts the size of the stable gauged Q-balls. For a given value

of the gauge coupling, the stable gauged Q-balls can only be realized in the region of charge $Q_s < Q < Q_{\max}$. The upper limit Q_{\max} and lower limit Q_s mainly comes from the stress stability and quantum stability criterion respectively. By using the thin-wall approximation, we show that the piecewise model can describe the basic properties of gauged Q-balls in FLSM model well. Based on this, we further give an approximately analytic evaluation of Q_{\max} by using the mapping method. We find the maximal charge is approximately $Q_{\max} \propto \tilde{g}^{-2}$ where \tilde{g} is the gauge coupling of the dark $U(1)$ symmetry. The constraint on the value of gauge coupling \tilde{g} is given by Eq. (5.30) if the gauged Q-balls are produced by the FOPT. We discuss the relic density of gauged Q-ball DM formed during electroweak FOPT. Even in the minimal SM plus singlet electroweak FOPT model, the gauged Q-balls can comprise all the observed DM. And we have found that in order to satisfy the relic abundance of DM, the original DM asymmetry surprisingly coincides with the observed large lepton number asymmetry. The charge and mass of gauged Q-ball DM can be varied by modifying the phase transition dynamics or the primordial DM asymmetry. Besides, we give combined constraints on the gauged Q-ball DM from DM direct detection (Mica, XENON1T, Ohya), and astronomical observations (CMB, neutron stars, white dwarfs). The formation process of gauged Q-ball DM during FOPT also provides phase transition GW signals which could be detected by future GW experiments such as LISA, TianQin, and Taiji. The phase transition dynamics in the early universe provides new formation mechanisms of various soliton DM or dynamical DM. For example, it is reasonable to discuss other species of soliton DM formed during FOPT, such as gauged Fermi-ball DM. The configuration of the Fermi-ball is different from the Q-ball because of the extra Fermi-gas degeneracy pressure. We leave these in our future works.

Acknowledgements: The authors thank Emin Nugaev, Julian Heeck, Michael Baker, Kiyoharu Kawana, Mikhail Smolyakov, Mikheil Sokhashvili, Yakov M. Shnir, Dmitry Levkov, Muhammad Fakhri Afif, Chris Verhaaren, Rebecca Riley, Sida Lu, Bingrong Yu, Jiahang Hu for helpful correspondence. This work was supported by the National Natural Science Foundation of China (NNSFC) under Grant No. 12205387, by Guangdong Major Project of Basic and Applied Basic Research (Grant No. 2019B030302001), and by KIAS Individual Grants under Grants No. PG021403 (PK).

References

- [1] G. Bertone and D. Hooper, *History of dark matter*, *Rev. Mod. Phys.* **90** (2018) 045002 [[1605.04909](#)].
- [2] A. Boveia et al., *Snowmass 2021 Dark Matter Complementarity Report*, [2211.07027](#).
- [3] A. Boveia et al., *Snowmass 2021 Cross Frontier Report: Dark Matter Complementarity (Extended Version)*, [2210.01770](#).
- [4] J. Cooley et al., *Report of the Topical Group on Particle Dark Matter for Snowmass 2021*, [2209.07426](#).
- [5] S. Baek, P. Ko and P. Wu, *Top-philic Scalar Dark Matter with a Vector-like Fermionic Top Partner*, *JHEP* **10** (2016) 117 [[1606.00072](#)].

- [6] S. Baek, P. Ko and P. Wu, *Heavy quark-philic scalar dark matter with a vector-like fermion portal*, *JCAP* **07** (2018) 008 [[1709.00697](#)].
- [7] T. Abe, J. Kawamura, S. Okawa and Y. Omura, *Dark matter physics, flavor physics and LHC constraints in the dark matter model with a bottom partner*, *JHEP* **03** (2017) 058 [[1612.01643](#)].
- [8] S. Khan, J. Kim and P. Ko, *Interplay between Higgs inflation and dark matter models with dark $U(1)$ gauge symmetry*, [2309.07839](#).
- [9] H. Baer, K.-Y. Choi, J.E. Kim and L. Roszkowski, *Dark matter production in the early Universe: beyond the thermal WIMP paradigm*, *Phys. Rept.* **555** (2015) 1 [[1407.0017](#)].
- [10] T. Lin, *Dark matter models and direct detection*, *PoS* **333** (2019) 009 [[1904.07915](#)].
- [11] S. Baek, P. Ko and W.-I. Park, *Hidden sector monopole, vector dark matter and dark radiation with Higgs portal*, *JCAP* **10** (2014) 067 [[1311.1035](#)].
- [12] A. Derevianko and M. Pospelov, *Hunting for topological dark matter with atomic clocks*, *Nature Phys.* **10** (2014) 933 [[1311.1244](#)].
- [13] E. Witten, *Cosmic Separation of Phases*, *Phys. Rev. D* **30** (1984) 272.
- [14] E. Krylov, A. Levin and V. Rubakov, *Cosmological phase transition, baryon asymmetry and dark matter Q -balls*, *Phys. Rev. D* **87** (2013) 083528 [[1301.0354](#)].
- [15] F.P. Huang and C.S. Li, *Probing the baryogenesis and dark matter relaxed in phase transition by gravitational waves and colliders*, *Phys. Rev. D* **96** (2017) 095028 [[1709.09691](#)].
- [16] S. Jiang, A. Yang, J. Ma and F.P. Huang, *Implication of nano-Hertz stochastic gravitational wave on dynamical dark matter through a dark first-order phase transition*, *Class. Quant. Grav.* **41** (2024) 065009 [[2306.17827](#)].
- [17] J.-P. Hong, S. Jung and K.-P. Xie, *Fermi-ball dark matter from a first-order phase transition*, *Phys. Rev. D* **102** (2020) 075028 [[2008.04430](#)].
- [18] K. Griest and M. Kamionkowski, *Unitarity Limits on the Mass and Radius of Dark Matter Particles*, *Phys. Rev. Lett.* **64** (1990) 615.
- [19] M.J. Baker, J. Kopp and A.J. Long, *Filtered Dark Matter at a First Order Phase Transition*, *Phys. Rev. Lett.* **125** (2020) 151102 [[1912.02830](#)].
- [20] D. Chway, T.H. Jung and C.S. Shin, *Dark matter filtering-out effect during a first-order phase transition*, *Phys. Rev. D* **101** (2020) 095019 [[1912.04238](#)].
- [21] G. Rosen, *Particlelike Solutions to Nonlinear Complex Scalar Field Theories with Positive-Definite Energy Densities*, *J. Math. Phys.* **9** (1968) 996.
- [22] S.R. Coleman, *Q -balls*, *Nucl. Phys. B* **262** (1985) 263.
- [23] K.-M. Lee, J.A. Stein-Schabes, R. Watkins and L.M. Widrow, *Gauged q Balls*, *Phys. Rev. D* **39** (1989) 1665.
- [24] G. Rosen, *Charged Particlelike Solutions to Nonlinear Complex Scalar Field Theories*, *J. Math. Phys.* **9** (1968) 999.
- [25] C.H. Lee and S.U. Yoon, *Existence and stability of gauged nontopological solitons*, *Mod. Phys. Lett. A* **6** (1991) 1479.

- [26] R. Friedberg, T.D. Lee and A. Sirlin, *A Class of Scalar-Field Soliton Solutions in Three Space Dimensions*, *Phys. Rev. D* **13** (1976) 2739.
- [27] H. Arodz and J. Lis, *Compact Q-balls and Q-shells in a scalar electrodynamics*, *Phys. Rev. D* **79** (2009) 045002 [[0812.3284](#)].
- [28] V. Benci and D. Fortunato, *On the existence of stable charged Q-balls*, *J. Math. Phys.* **52** (2011) 093701 [[1011.5044](#)].
- [29] V. Benci and D. Fortunato, *Hylomorphic solitons and charged Q-balls: Existence and stability*, *Chaos Solitons Fractals* **58** (2014) 1 [[1212.3236](#)].
- [30] V. Dzhuhashaliev and K.G. Zloshchastiev, *Singularity-free model of electric charge in physical vacuum: Non-zero spatial extent and mass generation*, *Central Eur. J. Phys.* **11** (2013) 325 [[1204.6380](#)].
- [31] I.E. Gulamov, E.Y. Nugaev and M.N. Smolyakov, *Theory of $U(1)$ gauged Q-balls revisited*, *Phys. Rev. D* **89** (2014) 085006 [[1311.0325](#)].
- [32] I.E. Gulamov, E.Y. Nugaev, A.G. Panin and M.N. Smolyakov, *Some properties of $U(1)$ gauged Q-balls*, *Phys. Rev. D* **92** (2015) 045011 [[1506.05786](#)].
- [33] E.Y. Nugaev and A.V. Shkerin, *Review of Nontopological Solitons in Theories with $U(1)$ -Symmetry*, *J. Exp. Theor. Phys.* **130** (2020) 301 [[1905.05146](#)].
- [34] A. Kusenko, *Solitons in the supersymmetric extensions of the standard model*, *Phys. Lett. B* **405** (1997) 108 [[hep-ph/9704273](#)].
- [35] A. Kusenko and M.E. Shaposhnikov, *Supersymmetric Q balls as dark matter*, *Phys. Lett. B* **418** (1998) 46 [[hep-ph/9709492](#)].
- [36] S. Kasuya, M. Kawasaki and M. Yamada, *Revisiting the gravitino dark matter and baryon asymmetry from Q-ball decay in gauge mediation*, *Phys. Lett. B* **726** (2013) 1 [[1211.4743](#)].
- [37] J.-P. Hong and M. Kawasaki, *New type of charged Q -ball dark matter in gauge mediated SUSY breaking models*, *Phys. Rev. D* **95** (2017) 123532 [[1702.00889](#)].
- [38] J.-P. Hong, M. Kawasaki and M. Yamada, *Charged Q-ball Dark Matter from B and L direction*, *JCAP* **08** (2016) 053 [[1604.04352](#)].
- [39] LISA collaboration, *Laser Interferometer Space Antenna*, [1702.00786](#).
- [40] TIANQIN collaboration, *TianQin: a space-borne gravitational wave detector*, *Class. Quant. Grav.* **33** (2016) 035010 [[1512.02076](#)].
- [41] Z.-C. Liang, Z.-Y. Li, J. Cheng, E.-K. Li, J.-d. Zhang and Y.-M. Hu, *Impact of combinations of time-delay interferometry channels on stochastic gravitational wave background detection*, *Phys. Rev. D* **107** (2023) 083033 [[2212.02852](#)].
- [42] W.-R. Hu and Y.-L. Wu, *The Taiji Program in Space for gravitational wave physics and the nature of gravity*, *Natl. Sci. Rev.* **4** (2017) 685.
- [43] V. Corbin and N.J. Cornish, *Detecting the cosmic gravitational wave background with the big bang observer*, *Class. Quant. Grav.* **23** (2006) 2435 [[gr-qc/0512039](#)].
- [44] N. Seto, S. Kawamura and T. Nakamura, *Possibility of direct measurement of the acceleration of the universe using 0.1-Hz band laser interferometer gravitational wave antenna in space*, *Phys. Rev. Lett.* **87** (2001) 221103 [[astro-ph/0108011](#)].

- [45] H. Kudoh, A. Taruya, T. Hiramatsu and Y. Himemoto, *Detecting a gravitational-wave background with next-generation space interferometers*, *Phys. Rev. D* **73** (2006) 064006 [[gr-qc/0511145](#)].
- [46] J. Heeck and M. Sokhashvili, *Revisiting the Friedberg–Lee–Sirlin soliton model*, *Eur. Phys. J. C* **83** (2023) 526 [[2303.09566](#)].
- [47] E. Pontón, Y. Bai and B. Jain, *Electroweak Symmetric Dark Matter Balls*, *JHEP* **09** (2019) 011 [[1906.10739](#)].
- [48] V. Loiko and Y. Shnir, *Q-balls in the $U(1)$ gauged Friedberg–Lee–Sirlin model*, *Phys. Lett. B* **797** (2019) 134810 [[1906.01943](#)].
- [49] V. Loiko and Y. Shnir, *Q-ball stress stability criterion in $U(1)$ gauged scalar theories*, *Phys. Rev. D* **106** (2022) 045021 [[2207.02646](#)].
- [50] M.P. Kinach and M.W. Choptuik, *Dynamical evolution of $U(1)$ gauged Q-balls in axisymmetry*, *Phys. Rev. D* **107** (2023) 035022 [[2211.11198](#)].
- [51] W.H. Press, S.A. Teukolsky, W.T. Vetterling and B.P. Flannery, *Numerical Recipes 3rd Edition: The Art of Scientific Computing*, Cambridge University Press, New York, NY, USA, 3 ed. (2007).
- [52] H.-K. Guo, K. Sinha, C. Sun, J. Swaim and D. Vagie, *Two-scalar Bose-Einstein condensates: from stars to galaxies*, *JCAP* **10** (2021) 028 [[2010.15977](#)].
- [53] A.G. Cohen, S.R. Coleman, H. Georgi and A. Manohar, *The Evaporation of Q Balls*, *Nucl. Phys. B* **272** (1986) 301.
- [54] M. Kawasaki and M. Yamada, *Q ball Decay Rates into Gravitinos and Quarks*, *Phys. Rev. D* **87** (2013) 023517 [[1209.5781](#)].
- [55] J.-P. Hong and M. Kawasaki, *Gauged Q-ball Decay Rates into Fermions*, *Phys. Rev. D* **96** (2017) 103526 [[1706.01651](#)].
- [56] M. Laue, *Zur Dynamik der Relativitätstheorie*, *Annalen Phys.* **340** (1911) 524.
- [57] I. Bialynicki-Birula, *Simple relativistic model of a finite size particle*, *Phys. Lett. A* **182** (1993) 346 [[nucl-th/9306006](#)].
- [58] M.V. Polyakov, *Generalized parton distributions and strong forces inside nucleons and nuclei*, *Phys. Lett. B* **555** (2003) 57 [[hep-ph/0210165](#)].
- [59] M. Mai and P. Schweitzer, *Energy momentum tensor, stability, and the D-term of Q-balls*, *Phys. Rev. D* **86** (2012) 076001 [[1206.2632](#)].
- [60] M.V. Polyakov and P. Schweitzer, *Forces inside hadrons: pressure, surface tension, mechanical radius, and all that*, *Int. J. Mod. Phys. A* **33** (2018) 1830025 [[1805.06596](#)].
- [61] I.A. Perevalova, M.V. Polyakov and P. Schweitzer, *On LHCb pentaquarks as a baryon- $\psi(2S)$ bound state: prediction of isospin- $\frac{3}{2}$ pentaquarks with hidden charm*, *Phys. Rev. D* **94** (2016) 054024 [[1607.07008](#)].
- [62] K.N. Anagnostopoulos, M. Axenides, E.G. Floratos and N. Tetradis, *Large gauged Q balls*, *Phys. Rev. D* **64** (2001) 125006 [[hep-ph/0109080](#)].
- [63] H. Ishihara and T. Ogawa, *Charge Screened Nontopological Solitons in a Spontaneously Broken $U(1)$ Gauge Theory*, *PTEP* **2019** (2019) 021B01 [[1811.10894](#)].

- [64] A.G. Panin and M.N. Smolyakov, *Problem with classical stability of $U(1)$ gauged Q -balls*, *Phys. Rev. D* **95** (2017) 065006 [[1612.00737](#)].
- [65] T.D. Lee and Y. Pang, *Nontopological solitons*, *Phys. Rept.* **221** (1992) 251.
- [66] N.G. Vakhitov and A.A. Kolokolov, *Stationary solutions of the wave equation in the medium with nonlinearity saturation*, .
- [67] V.G. Makhankov, *Dynamics of classical solitons (in non-integrable systems)*, *Physics Reports* **35** (1978) 1.
- [68] D. Levkov, E. Nugaev and A. Popescu, *The fate of small classically stable Q -balls*, *JHEP* **12** (2017) 131 [[1711.05279](#)].
- [69] J. Heeck, A. Rajaraman, R. Riley and C.B. Verhaaren, *Mapping Gauged Q -Balls*, *Phys. Rev. D* **103** (2021) 116004 [[2103.06905](#)].
- [70] I.E. Gulamov, E.Y. Nugaev and M.N. Smolyakov, *Analytic Q -ball solutions and their stability in a piecewise parabolic potential*, *Phys. Rev. D* **87** (2013) 085043 [[1303.1173](#)].
- [71] E. Kim and E. Nugaev, *Effectively flat potential in the Friedberg-Lee-Sirlin model*, [2309.09661](#).
- [72] J. Heeck, A. Rajaraman, R. Riley and C.B. Verhaaren, *Understanding Q -Balls Beyond the Thin-Wall Limit*, *Phys. Rev. D* **103** (2021) 045008 [[2009.08462](#)].
- [73] J.R. Espinosa and M. Quiros, *The Electroweak phase transition with a singlet*, *Phys. Lett. B* **305** (1993) 98 [[hep-ph/9301285](#)].
- [74] P. Bandyopadhyay and S. Jangid, *Discerning singlet and triplet scalars at the electroweak phase transition and gravitational wave*, *Phys. Rev. D* **107** (2023) 055032 [[2111.03866](#)].
- [75] L. Dolan and R. Jackiw, *Symmetry Behavior at Finite Temperature*, *Phys. Rev. D* **9** (1974) 3320.
- [76] A. Salvio, A. Strumia, N. Tetradis and A. Urbano, *On gravitational and thermal corrections to vacuum decay*, *JHEP* **09** (2016) 054 [[1608.02555](#)].
- [77] M.S. Turner, E.J. Weinberg and L.M. Widrow, *Bubble nucleation in first order inflation and other cosmological phase transitions*, *Phys. Rev. D* **46** (1992) 2384.
- [78] J. Ellis, M. Lewicki and J.M. No, *On the Maximal Strength of a First-Order Electroweak Phase Transition and its Gravitational Wave Signal*, *JCAP* **04** (2019) 003 [[1809.08242](#)].
- [79] A. Megevand and S. Ramirez, *Bubble nucleation and growth in very strong cosmological phase transitions*, *Nucl. Phys. B* **919** (2017) 74 [[1611.05853](#)].
- [80] A. Kobakhidze, C. Lagger, A. Manning and J. Yue, *Gravitational waves from a supercooled electroweak phase transition and their detection with pulsar timing arrays*, *Eur. Phys. J. C* **77** (2017) 570 [[1703.06552](#)].
- [81] J. Ellis, M. Lewicki and J.M. No, *Gravitational waves from first-order cosmological phase transitions: lifetime of the sound wave source*, *JCAP* **07** (2020) 050 [[2003.07360](#)].
- [82] X. Wang, F.P. Huang and X. Zhang, *Phase transition dynamics and gravitational wave spectra of strong first-order phase transition in supercooled universe*, *JCAP* **05** (2020) 045 [[2003.08892](#)].
- [83] C.L. Wainwright, *CosmoTransitions: Computing Cosmological Phase Transition*

Temperatures and Bubble Profiles with Multiple Fields, *Comput. Phys. Commun.* **183** (2012) 2006 [[1109.4189](#)].

- [84] W. Chao, X.-F. Li and L. Wang, *Filtered pseudo-scalar dark matter and gravitational waves from first order phase transition*, *JCAP* **06** (2021) 038 [[2012.15113](#)].
- [85] S. Jiang, F.P. Huang and C.S. Li, *Hydrodynamic effects on the filtered dark matter produced by a first-order phase transition*, *Phys. Rev. D* **108** (2023) 063508 [[2305.02218](#)].
- [86] G.D. Moore and T. Prokopec, *How fast can the wall move? A Study of the electroweak phase transition dynamics*, *Phys. Rev. D* **52** (1995) 7182 [[hep-ph/9506475](#)].
- [87] B. Laurent and J.M. Cline, *First principles determination of bubble wall velocity*, *Phys. Rev. D* **106** (2022) 023501 [[2204.13120](#)].
- [88] M. Lewicki, M. Merchand and M. Zych, *Electroweak bubble wall expansion: gravitational waves and baryogenesis in Standard Model-like thermal plasma*, *JHEP* **02** (2022) 017 [[2111.02393](#)].
- [89] X. Wang, F.P. Huang and X. Zhang, *Bubble wall velocity beyond leading-log approximation in electroweak phase transition*, [2011.12903](#).
- [90] S. Jiang, F.P. Huang and X. Wang, *Bubble wall velocity during electroweak phase transition in the inert doublet model*, *Phys. Rev. D* **107** (2023) 095005 [[2211.13142](#)].
- [91] G.C. Dorsch, S.J. Huber and T. Konstandin, *A sonic boom in bubble wall friction*, *JCAP* **04** (2022) 010 [[2112.12548](#)].
- [92] S. De Curtis, L.D. Rose, A. Guiggiani, A.G. Muyor and G. Panico, *Bubble wall dynamics at the electroweak phase transition*, *JHEP* **03** (2022) 163 [[2201.08220](#)].
- [93] W.-Y. Ai, B. Laurent and J. van de Vis, *Model-independent bubble wall velocities in local thermal equilibrium*, *JCAP* **07** (2023) 002 [[2303.10171](#)].
- [94] D.E. Kaplan, M.A. Luty and K.M. Zurek, *Asymmetric Dark Matter*, *Phys. Rev. D* **79** (2009) 115016 [[0901.4117](#)].
- [95] A. Falkowski, J.T. Ruderman and T. Volansky, *Asymmetric Dark Matter from Leptogenesis*, *JHEP* **05** (2011) 106 [[1101.4936](#)].
- [96] A. Matsumoto et al., *EMPRESS. VIII. A New Determination of Primordial He Abundance with Extremely Metal-poor Galaxies: A Suggestion of the Lepton Asymmetry and Implications for the Hubble Tension*, *Astrophys. J.* **941** (2022) 167 [[2203.09617](#)].
- [97] D. Borah and A. Dasgupta, *Large neutrino asymmetry from TeV scale leptogenesis*, *Phys. Rev. D* **108** (2023) 035015 [[2206.14722](#)].
- [98] Y. ChoeJo, K. Enomoto, Y. Kim and H.-S. Lee, *Second leptogenesis: Unraveling the baryon-lepton asymmetry discrepancy*, *JHEP* **03** (2024) 003 [[2311.16672](#)].
- [99] J. McDonald, *Naturally large cosmological neutrino asymmetries in the MSSM*, *Phys. Rev. Lett.* **84** (2000) 4798 [[hep-ph/9908300](#)].
- [100] M. Kawasaki and K. Murai, *Lepton asymmetric universe*, *JCAP* **08** (2022) 041 [[2203.09713](#)].
- [101] PARTICLE DATA GROUP collaboration, *Review of Particle Physics*, *Phys. Rev. D* **98** (2018) 030001.

- [102] S.J. Huber and T. Konstandin, *Production of gravitational waves in the nMSSM*, *JCAP* **05** (2008) 017 [[0709.2091](#)].
- [103] PLANCK collaboration, *Planck 2018 results. VI. Cosmological parameters*, *Astron. Astrophys.* **641** (2020) A6 [[1807.06209](#)].
- [104] J. McDonald, *Gauge singlet scalars as cold dark matter*, *Phys. Rev. D* **50** (1994) 3637 [[hep-ph/0702143](#)].
- [105] D. Curtin, P. Meade and C.-T. Yu, *Testing Electroweak Baryogenesis with Future Colliders*, *JHEP* **11** (2014) 127 [[1409.0005](#)].
- [106] F.P. Huang, P.-H. Gu, P.-F. Yin, Z.-H. Yu and X. Zhang, *Testing the electroweak phase transition and electroweak baryogenesis at the LHC and a circular electron-positron collider*, *Phys. Rev. D* **93** (2016) 103515 [[1511.03969](#)].
- [107] F.P. Huang, Y. Wan, D.-G. Wang, Y.-F. Cai and X. Zhang, *Hearing the echoes of electroweak baryogenesis with gravitational wave detectors*, *Phys. Rev. D* **94** (2016) 041702 [[1601.01640](#)].
- [108] C. Dvorkin, K. Blum and M. Kamionkowski, *Constraining Dark Matter-Baryon Scattering with Linear Cosmology*, *Phys. Rev. D* **89** (2014) 023519 [[1311.2937](#)].
- [109] D.M. Jacobs, G.D. Starkman and B.W. Lynn, *Macro Dark Matter*, *Mon. Not. Roy. Astron. Soc.* **450** (2015) 3418 [[1410.2236](#)].
- [110] XENON collaboration, *Dark Matter Search Results from a One Ton-Year Exposure of XENON1T*, *Phys. Rev. Lett.* **121** (2018) 111302 [[1805.12562](#)].
- [111] M. Clark, A. Depoian, B. Elshimy, A. Kopec, R.F. Lang, S. Li et al., *Direct Detection Limits on Heavy Dark Matter*, *Phys. Rev. D* **102** (2020) 123026 [[2009.07909](#)].
- [112] P.B. Price and M.H. Salamon, *Search for Supermassive Magnetic Monopoles Using Mica Crystals*, *Phys. Rev. Lett.* **56** (1986) 1226.
- [113] P.B. Price, *Limits on Contribution of Cosmic Nuclearites to Galactic Dark Matter*, *Phys. Rev. D* **38** (1988) 3813.
- [114] A. Bhoonah, J. Bramante, B. Courtman and N. Song, *Etched plastic searches for dark matter*, *Phys. Rev. D* **103** (2021) 103001 [[2012.13406](#)].
- [115] P.W. Graham, R. Janish, V. Narayan, S. Rajendran and P. Riggins, *White Dwarfs as Dark Matter Detectors*, *Phys. Rev. D* **98** (2018) 115027 [[1805.07381](#)].
- [116] J. Singh Sidhu and G.D. Starkman, *Reconsidering astrophysical constraints on macroscopic dark matter*, *Phys. Rev. D* **101** (2020) 083503 [[1912.04053](#)].
- [117] S.J. Huber and T. Konstandin, *Gravitational Wave Production by Collisions: More Bubbles*, *JCAP* **09** (2008) 022 [[0806.1828](#)].
- [118] C. Caprini et al., *Science with the space-based interferometer eLISA. II: Gravitational waves from cosmological phase transitions*, *JCAP* **04** (2016) 001 [[1512.06239](#)].
- [119] M. Hindmarsh, S.J. Huber, K. Rummukainen and D.J. Weir, *Shape of the acoustic gravitational wave power spectrum from a first order phase transition*, *Phys. Rev. D* **96** (2017) 103520 [[1704.05871](#)].
- [120] P. Binetruy, A. Bohe, C. Caprini and J.-F. Dufaux, *Cosmological Backgrounds of Gravitational Waves and eLISA/NGO: Phase Transitions, Cosmic Strings and Other Sources*, *JCAP* **06** (2012) 027 [[1201.0983](#)].